

A global-local approach for hydraulic phase-field fracture in poroelastic media

Fadi Aldakheel^a, Nima Noii^{b,1}, Thomas Wick^{b,c}, Peter Wriggers^{a,c}

^a Institute of Continuum Mechanics
Leibniz Universität Hannover, Appelstrasse 11, 30167 Hannover, Germany

^b Institute of Applied Mathematics
Leibniz Universität Hannover, Welfengarten 1, 30167 Hannover, Germany

^c Cluster of Excellence PhoenixD (Photonics, Optics, and Engineering - Innovation Across Disciplines) Leibniz Universität Hannover, Germany

Abstract

In this work, phase-field modeling of hydraulic fractures in porous media is extended towards a global-local approach. Therein, the failure behavior is solely analyzed in a (small) local domain. In the surrounding medium, a simplified and linearized system of equations is solved. Both domains are coupled by Robin-type interface conditions. The fracture(s) inside the local domain are allowed to propagate and consequently both subdomains change within time. Here, a predictor-corrector strategy is adopted in which the local domain is dynamically adjusted to the current fracture pattern. The resulting framework is algorithmically described in detail and substantiated with some numerical tests.

Keywords: Global-local methods, phase-field approach, hydraulic fracture, mesh adaptivity, dual mortar method, fluid-saturated porous media, finite strains.

1. Introduction

In recent years, several pressurized [11, 52, 51, 61, 37, 38, 58, 55] and fluid-filled [50, 65, 39, 48, 47, 24, 35, 36, 43, 60, 41, 15, 42, 16, 66, 6] phase-field fracture formulations have been proposed in the literature. These studies range from modeling of pressurized and fluid-filled fractures, mathematical analysis, numerical modeling and simulations up to high-performance parallel computations. Recently various extensions towards multi-physics phase-field fracture in porous media have been proposed in which various phenomena couple as for instance proppant [41], two-phase flow formulations [40] or given temperature variations [55]. All these examples demonstrate the potential of phase-field for crack propagation.

Phase-field fracture is a regularized approach, which has advantages and shortcomings. The first advantage is a continuum description based on first physical principles to determine the unknown crack path [27, 10, 46] and the computation of curvilinear and complex crack patterns. The model allows for nucleation, branching, merging and post-processing of certain quantities such that stress intensity factors become redundant. Therefore, easy handling of fracture networks in possibly and highly heterogeneous media can be treated. The formulation being described in a variational framework allows finite

¹Corresponding author.

E-mail addresses: aldakheel@ikm.uni-hannover.de (F. Aldakheel); noii@ifam.uni-hannover.de (N. Noii); thomas.wick@ifam.uni-hannover.de (T. Wick); wriggers@ikm.uni-hannover.de (P. Wriggers).

element discretizations and corresponding analyses. The mathematical model permits any dimension, thus phase-field fracture applies conveniently to three-dimensional simulations. On the energy level, the formulation is non-convex constituting a challenge for both theory and design of numerical algorithms. A second challenge is the computational cost. Various solutions have been proposed so far; namely staggered approaches (alternating minimization) [9, 13, 14], stabilized staggered techniques [12], quasi-monolithic approaches [37] (possibly with sub-iterations [44]), or fully monolithic approaches [29, 64, 63]. Adaptive mesh refinement was proposed to reduce the computational costs [13, 37, 7, 62]. A related technique that has the potential to treat large-scale problems is a global-local technique proposed in [30]. Recently this was extended to a framework in which the local domain is dynamically updated according to the propagating fracture path [54]. The need for such framework can be found in multiscale porous media applications [18, 19] or in which a localized fracture occurs in a (big) reservoir [65, 32].

The last two references are the motivation for the present work. Here, we extend the adaptive global-local phase-field fracture approach [54] to porous media applications with hydraulic fractures. We first extend our model towards large strain formulations, in line with [1, 3, 22, 49]. Previous studies only concentrated on small strain applications. Then, the coupled multiphysics fracture framework is carefully derived. Both subdomains will be coupled via Robin-type interface conditions, see [54]. This leads to Lagrange multiplier formulations that are demanding from a mathematical point of view as well as in the implementation, see for example [68, 69, 67, 57]. A future rigorous numerical analysis of our global-local approach can be achieved with similar methodologies as used in [33, 31]. In particular, our formulation can deal with non-matching grids at the interface, which is very interesting for cases towards practical field problems as mentioned in [65, 32] in which possibly various programming codes must be coupled. On the fine-scale level all (nonlinear) equations are solved. On the global level, only coarse representations of the pressure and crack phase-field are considered. As mentioned in the previous descriptions and references such multiphysics fracture formulations are challenging from a mathematical and numerical point of view. For these reasons, we concentrate in this paper on careful algorithmic descriptions including supporting numerical simulations. Here, our emphasis is on results, demonstrating the computational convergence properties of our proposed numerical schemes. A rigorous numerical analysis must be left for future work.

The outline of this paper is as follows: In Section 2, the governing equations are described. Then, in Section 3, the extension to a global-local formulation for pressurized fractures is derived. Therein, the Robin-type interface conditions are carefully discussed. This is followed by the final global-local algorithm. Afterward, we also discuss the dynamic choice of the local domains with the help of a predictor-corrector scheme. In Section 4 some numerical tests are carried out in order to substantiate our algorithmic developments.

2. Phase-field modeling of hydraulic fracture

This section outlines a theory of hydraulic phase-field fracture in poroelastic media undergoing finite strains. The constitutive formulations are based on three governing equations for the mechanical deformation, fluid pressure and the crack phase-field. Strong and weak formulations of the multi-physics problem are introduced. Furthermore the framework is algorithmically described, resulting in the so-called *single-scale domain* for-

mulations.

2.1. Governing equations

Consider $\mathcal{B} \in \mathcal{R}^\delta$ to be a material body (solid in the reference configuration) and denote $\partial\mathcal{B}$ as its boundary with dimension $\delta = 2, 3$ in space and time $t \in \mathcal{T} = [0, T]$. We assume Dirichlet boundary conditions on $\partial_D\mathcal{B}$ and Neumann conditions on $\partial_N\mathcal{B} := \Gamma_N \cup \mathcal{C}$, where Γ_N denotes the outer domain boundary. The lower dimensional curved surface $\mathcal{C} \in \mathcal{R}^{\delta-1}$ is the crack boundary, as illustrated in Fig. 1.

The boundary-value-problem BVP for the coupled problem of fluid-saturated porous media at fracture is a coupled three-field problem. It is characterized at material points $\mathbf{X} \in \mathcal{B}$ by the deformation map $\boldsymbol{\varphi}(\mathbf{X}, t)$ of the solid, the fluid pressure field $p(\mathbf{X}, t)$ and the crack phase-field $d(\mathbf{X}, t)$ defined as

$$\boldsymbol{\varphi} : \begin{cases} \mathcal{B} \times \mathcal{T} \rightarrow \mathcal{R}^\delta \\ (\mathbf{X}, t) \mapsto \mathbf{x} = \boldsymbol{\varphi}(\mathbf{X}, t) \end{cases}, \quad p : \begin{cases} \mathcal{B} \times \mathcal{T} \rightarrow \mathcal{R} \\ (\mathbf{X}, t) \mapsto p(\mathbf{X}, t) \end{cases}, \quad d : \begin{cases} \mathcal{B} \times \mathcal{T} \rightarrow [0, 1] \\ (\mathbf{X}, t) \mapsto d(\mathbf{X}, t) \end{cases}, \quad (1)$$

with $\dot{d} \geq 0$. The position of a material point in the deformed configuration is depicted as $\mathbf{x} = \mathbf{X} + \mathbf{u}(\mathbf{X}, t)$ where $\mathbf{u}(\mathbf{X}, t)$ is the displacement field. The crack phase-field $d(\mathbf{X}, t) = 0$ (light gray color) and $d(\mathbf{X}, t) = 1$ (red color) refer to the unbroken and fully fractured state of the material respectively, as visualized in Fig. 1. The fracture surface \mathcal{C} is approximated in $\mathcal{B}_L \subset \mathcal{B}$ the so-called *local domain*. The intact region with no fracture is denoted as *complementary domain* $\mathcal{B}_C := \mathcal{B} \setminus \mathcal{B}_L \subset \mathcal{B}$, such that $\mathcal{B}_C \cup \mathcal{B}_L =: \mathcal{B}$ and $\mathcal{B}_C \cap \mathcal{B}_L = \emptyset$. We note that \mathcal{B}_L , the domain in which the smeared crack phase-field is approximated, and its boundary $\partial\mathcal{B}_L$ depend on the choice of the phase-field regularization parameter $l > 0$.

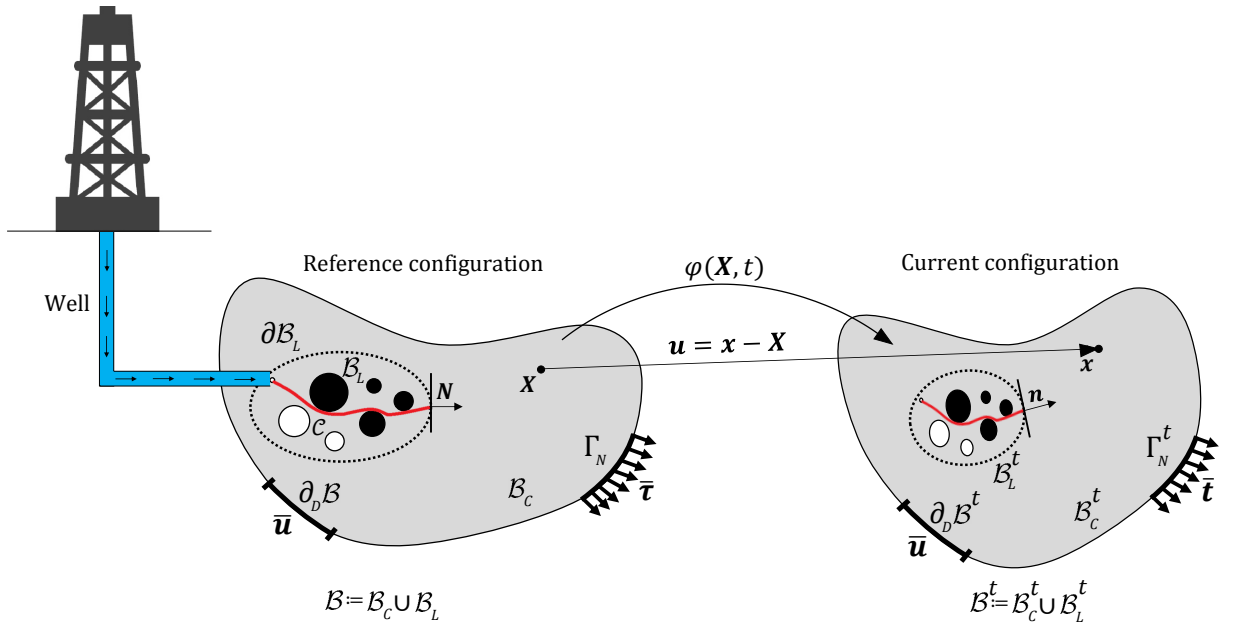


Figure 1: Setup of the notation: the unbroken domain is denoted by \mathcal{B}_C and \mathcal{C} is the crack phase-field. The smeared crack phase-field is approximated by the domain \mathcal{B}_L . The whole domain is defined as a close subset as $\mathcal{B} := \mathcal{B}_C \cup \mathcal{B}_L$. The fracture boundary is $\partial\mathcal{B}_L$ and the outer boundary of the domain is $\partial\mathcal{B}$. Blue color refer to the injected fluid through the well drilling and injection.

The material deformation gradient of the solid is defined by $\mathbf{F} := \nabla \boldsymbol{\varphi}(\mathbf{X}, t) = \text{Grad} \boldsymbol{\varphi}$ with the Jacobian $J := \det[\mathbf{F}] > 0$ and the right Cauchy-Green tensor $\mathbf{C} = \mathbf{F}^T \mathbf{F}$. The solid is loaded by prescribed deformations and external traction on the boundary, defined by time-dependent Dirichlet- and Neumann conditions

$$\boldsymbol{\varphi} = \bar{\boldsymbol{\varphi}}(\mathbf{X}, t) \text{ on } \partial_D \mathcal{B} \quad \text{and} \quad \mathbf{P} \mathbf{N} = \bar{\boldsymbol{\tau}}(\mathbf{X}, t) \text{ on } \partial_N \mathcal{B}, \quad (2)$$

where \mathbf{N} is the outward unit normal vector and $\bar{\boldsymbol{\tau}}$ is the prescribed traction vector at the surface $\partial \mathcal{B}$ of the undeformed configuration. The first Piola-Kirchhoff stress tensor \mathbf{P} is the thermodynamic dual to \mathbf{F} .

The solid has to satisfy the equation of equilibrium, representing the *first* partial differential equation PDE for the coupled problem as

$$\text{Div } \mathbf{P} + \bar{\mathbf{b}} = \mathbf{0} \quad (3)$$

where dynamic effects are neglected and $\bar{\mathbf{b}}$ is the given body force.

For the constitutive modeling of poromechanics, we proceed with a *biphasic* fully saturated porous material, consisting of a pore fluid and a solid matrix material. A local volume element dV in the undeformed reference configuration can be decomposed into a fluid dV_F and a solid dV_S part. Thereby the volume fraction can be defined via $n_\alpha := dV_\alpha/dV$, where $\alpha = \{S, F\}$. The *saturation condition* for the case of a fully saturated porous medium is given by

$$\sum_{\alpha} n_{\alpha} = n_F + n_S = 1, \quad (4)$$

where $n_F(\mathbf{X}, t)$ represents the porosity, i.e. the volume occupied by the fluid is *same as* the pore volume. Note that in the *fracture region* where

$$d = 1 \quad \text{yields} \quad n_S = 0 \quad \text{and} \quad n_F = 1. \quad (5)$$

The volume fraction in porous media relates the real density (material, effective, intrinsic) $\rho_{\alpha R}$ to the partial density ρ_α by

$$\rho_\alpha = n_\alpha \rho_{\alpha R} \quad \text{with} \quad \rho_{\alpha R} := dm_\alpha/dV_\alpha \quad \text{and} \quad \rho_\alpha := dm_\alpha/dV, \quad (6)$$

where dm_α is the mass of the phase α . Thus, the overall density can be expressed as $\rho = \sum_{\alpha} n_{\alpha} \rho_{\alpha R}$. A review on the foundations and applications of porous materials can be seen in the pioneering works [8, 17, 21, 23, 56, 45]. The fluid volume fraction (porosity) n_F is linked to the fluid volume ratio θ (fluid content) per unit volume of the undeformed reference configuration \mathcal{B} via

$$n_F = n_{F,0} + \theta, \quad (7)$$

for constant fluid material density, where $n_{F,0}$ is the initial porosity. In the constitutive modeling θ describes the *first local internal* variable (history field). The evolution of this fluid volume ratio $\dot{\theta} = \dot{n}_F$ is derived by the fluid pressure field p . The boundary conditions for the pressure are determined as follows

$$p = \bar{p}(\mathbf{X}, t) \text{ on } \partial_D \mathcal{B} \quad \text{and} \quad \mathcal{F} \cdot \mathbf{N} = \bar{f}(\mathbf{X}, t) \text{ on } \partial_N \mathcal{B}, \quad (8)$$

in terms of the material fluid volume flux vector \mathcal{F} and the prescribed fluid pressure \bar{p} and fluid transport \bar{f} . The initial condition for the fluid volume ratio is set to $\theta(\mathbf{X}, t_0) = 0$ yields $n_F = n_{F,0}$ in \mathcal{B} . Furthermore, the fluid flux vector in (8) is linked to the negative material gradient of the fluid pressure via the permeability, according to Darcy-type fluid transport as

$$\mathcal{F} := -\mathbf{K}(\mathbf{F}, d) \nabla p, \quad (9)$$

where the permeability tensor \mathbf{K} depends on the material deformation gradient \mathbf{F} and the crack phase-field d . It is decomposed into a *Darcy-type flow for an unbroken porous medium* \mathbf{K}_{Darcy} and a *Poiseuille-type flow in a fully fractured material* \mathbf{K}_{crack} defined as

$$\begin{aligned} \mathbf{K}(\mathbf{F}, d) &= \mathbf{K}_{Darcy}(\mathbf{F}) + d^\zeta \mathbf{K}_{frac}(\mathbf{F}), \\ \mathbf{K}_{Darcy}(\mathbf{F}) &= \frac{K}{\eta_F} J \mathbf{C}^{-1}, \\ \mathbf{K}_{frac}(\mathbf{F}) &= K_c \omega^2 J [\mathbf{C}^{-1} - \mathbf{C}^{-1} \mathbf{n} \otimes \mathbf{C}^{-1} \mathbf{n}], \end{aligned} \quad (10)$$

as outlined in [6, 47], where K is the intrinsic permeability in an isotropic pore space, $\mathbf{n} = \nabla d / |\nabla d|$ is the normal of material crack surface, η_F is the dynamic fluid viscosity, $\zeta \geq 1$ is a permeability transition exponent and K_c is the spatial permeability in fracture. An estimation for the crack width is provided by $\omega = (\lambda_\perp - 1)h_e$ in terms of the stretch perpendicular to the crack $\lambda_\perp^2 = \nabla d \cdot \nabla d / \nabla d \cdot \mathbf{C}^{-1} \cdot \nabla d$ and the characteristic element length h_e .

The fluid has to satisfy the balance of fluid mass, reflecting the *second* PDE for the coupled problem as

$$\dot{n}_F - \bar{r}_F + \text{Div}[\mathcal{F}] = 0 \quad (11)$$

with a prescribed fluid source \bar{r}_F per unit volume of the reference configuration \mathcal{B} , which describes the injection process in hydraulic fracturing.

For the phase-field problem, a sharp-crack surface topology $\mathcal{C} \rightarrow \mathcal{C}_l$ is regularized by the crack surface functional as outlined in [2, 4]

$$\mathcal{C}_l(d) = \int_{\mathcal{B}} \gamma_l(d, \nabla d) dV \quad \text{with} \quad \gamma_l(d, \nabla d) = \frac{1}{2l} d^2 + \frac{l}{2} |\nabla d|^2, \quad (12)$$

based on the crack surface density function γ_l per unit volume of the solid and the fracture length scale parameter l that governs the regularization, as plotted in Fig. 1. To describe a purely geometric approach to phase-field fracture, the regularized crack phase-field d is obtained by a minimization principle of diffusive crack topology

$$d = \text{Arg}\{\inf_d \mathcal{C}_l(d)\} \quad \text{with} \quad d = 1 \text{ on } \mathcal{C} \subset \mathcal{B}, \quad (13)$$

yielding the Euler equation $d - l^2 \Delta d = 0$ in \mathcal{B} along with the Neumann-type boundary condition $\nabla d \cdot \mathbf{N} = 0$ on $\partial \mathcal{B}$. Evolution of the regularized crack surface functional (12) can be driven by the constitutive functions as outlined in [3, 46], postulating a global evolution equation of regularized crack surface as

$$\frac{d}{dt} \mathcal{C}_l(d) := \frac{1}{l} \int_{\mathcal{B}} [(1-d)\mathcal{H} - \eta \dot{d}] \dot{d} dV \geq 0, \quad (14)$$

where $\eta \geq 0$ is a material parameter that characterizes the artificial/numerical viscosity of the crack propagation. The crack driving force

$$\mathcal{H} = \max_{s \in [0, t]} D(\mathbf{x}, s) \geq 0, \quad (15)$$

is introduced as the *second local history variable* that accounts for the irreversibility of the phase-field evolution by filtering out a maximum value of what is known as the crack driving state function D . Then the evolution statement (14) provides the local equation for the evolution of the crack phase-field in the domain \mathcal{B} along with its homogeneous Neumann boundary condition as

$$[d - l^2 \Delta d] + \eta \dot{d} + (d - 1)\mathcal{H} = 0 \quad (16)$$

with $\nabla d \cdot \mathbf{N} = 0$ on $\partial\mathcal{B}$. It represents the *third* PDE for the coupled problem.

2.2. Constitutive functions

The multi-physics problem is based on three primary fields to characterize the hydro-poro-elasticity of fluid-saturated porous media as

$$\text{Global Primary Fields : } \mathfrak{U} := \{\boldsymbol{\varphi}, p, d\}, \quad (17)$$

the deformation map $\boldsymbol{\varphi}$, the pressure field p and the crack phase-field d . The constitutive approach to hydraulic phase-field fracture in poroelastic media focuses on the set

$$\text{Constitutive State Variables : } \mathfrak{C} := \{\mathbf{F}, \theta, d, \nabla d\}, \quad (18)$$

reflecting a combination of poro-elasticity with a first-order gradient damage modeling. It is based on the definition of a pseudo-energy density per unit volume contains the sum

$$W(\mathfrak{C}) = W_{elas}(\mathbf{F}, d) + W_{fluid}(\mathbf{F}, \theta) + W_{frac}(d, \nabla d) \quad (19)$$

of a degrading elastic part W_{elas} and a contribution due to fluid W_{fluid} and fracture W_{frac} that contain the accumulated dissipative energy. The elastic contribution is modeled with a Neo-Hookean strain energy function for a homogeneous compressible isotropic elastic solid

$$W_{elas}(\mathbf{F}, d) = g(d) \psi_{elas}(\mathbf{F}) \quad \text{with} \quad \psi_{elas}(\mathbf{F}) = \frac{\mu}{2} \left[(\mathbf{F} : \mathbf{F} - 3) + \frac{2}{\beta} (J^{-\beta} - 1) \right], \quad (20)$$

in terms of the shear modulus μ and the parameter $\beta = 2\nu/(1 - 2\nu)$ with the Poisson number ν . The function $g(d) = (1 - d)^2$ models the degradation of the elastic energy of the solid due to fracture. It interpolates between the unbroken response for $d = 0$ and the fully broken state at $d = 1$ by satisfying the constraints $g(0) = 1$, $g(1) = 0$, $g'(d) \leq 0$ and $g'(1) = 0$. The fluid contribution is assumed to have the form

$$W_{fluid}(\mathbf{F}, \theta) = \frac{M}{2} \left[B^2 (J - 1)^2 - 2\theta B (J - 1) + \theta^2 \right], \quad (21)$$

in terms of the Biot's coefficient B and Biot's modulus M . Following the Coleman-Noll procedure, the fluid pressure p and the first Piola-Kirchoff stress tensor \mathbf{P} are obtained from the pseudo-energy density function W in (19) for isotropic material behavior as

$$p(\mathbf{F}, \theta) := \frac{\partial W}{\partial \theta} = \theta M - MB(J - 1), \quad (22)$$

$$\mathbf{P}(\mathbf{F}, p, d) := \frac{\partial W}{\partial \mathbf{F}} = g(d)\mathbf{P}_{eff}(\mathbf{F}) - BpJ\mathbf{F}^{-T} \quad \text{with} \quad \mathbf{P}_{eff} = \mu[\mathbf{F} - J^{-\beta}\mathbf{F}^{-T}],$$

where the stress tensor is additively decomposed into an effective part \mathbf{P}_{eff} and a pressure part according to the classical Terzaghi split, as outlined in [59, 20]. Using the pressure definition in (22)₁ and the second PDE in (11) along with (7), the balance of mass is modified as follows

$$\frac{\dot{p}}{M} + B\dot{J} - \bar{r}_F + \text{Div}[\mathcal{F}] = 0, \quad (23)$$

which now depends on the fluid pressure p and the deformation $\boldsymbol{\varphi}$.

The fracture part of pseudo-energy density (19) is modeled by

$$W_{frac}(d, \nabla d) = [1 - g(d)] \psi_c + 2\psi_c l \gamma_l(d, \nabla d), \quad (24)$$

where $\psi_c > 0$ is a critical fracture energy. It is defined in terms of the critical effective stress σ_c or the Griffith's energy release rate G_c , as outlined in [2]

$$\psi_c = \frac{\sigma_c^2}{2E} = \frac{3}{8l\sqrt{2}}G_c. \quad (25)$$

By taking the variational derivative $\delta_d W$ of (19) with some manipulation as documented in [5], the third PDE in (16) yields for the rate-independent setting as follows

$$2\psi_c[d - l^2\Delta d] + 2(d - 1)\mathcal{H} = 0, \quad (26)$$

in terms of the history field \mathcal{H} , introduced in (15). The crack driving state function D is defined by

$$D := \left\langle \psi_{elas}(\mathbf{F}(\mathbf{X}, s)) - \psi_c \right\rangle_+ \geq 0, \quad (27)$$

with the Macaulay bracket $\langle x \rangle_+ := (x + |x|)/2$, that ensures the irreversibility of the crack evolution.

2.3. Weak formulations for the coupled problem

The update of the primary fields \mathbf{u} in (17) in a typical time increment $[t_n, t_{n+1}]$ with time step $\Delta t > 0$ is governed by three PDEs in (3), (23) and (16) in a strong form setting. Next, we define three test functions for the deformation $\delta\boldsymbol{\varphi}(\mathbf{X}) \in \{\mathbf{H}^1(\mathcal{B})^\delta : \delta\boldsymbol{\varphi} = \mathbf{0} \text{ on } \partial_D\mathcal{B}\}$, fluid pressure $\delta p(\mathbf{X}) \in \{H^1(\mathcal{B}) : \delta p = 0 \text{ on } \partial_D\mathcal{B}\}$ and crack phase-field $\delta d(\mathbf{X}) \in H^1(\mathcal{B})$. The weak formulations for the above introduced three PDEs of the coupled poro-elastic media problem at fracture are derived from a standard Galerkin procedure as

$$\begin{aligned} G_\varphi(\mathbf{u}, \delta\boldsymbol{\varphi}) &= \int_{\mathcal{B}} [\mathbf{P} : \nabla \delta\boldsymbol{\varphi} - \bar{\mathbf{b}} \cdot \delta\boldsymbol{\varphi}] dV - \int_{\partial_N\mathcal{B}} \bar{\boldsymbol{\tau}} \cdot \delta\boldsymbol{\varphi} dA = 0, \\ G_p(\mathbf{u}, \delta p) &= \int_{\mathcal{B}} \left[\left(\frac{1}{M}(p - p_n) + B(J - J_n) - \Delta t \bar{r}_F \right) \delta p + (\Delta t \mathbf{K} \nabla p) \cdot \nabla \delta p \right] dV \\ &\quad + \int_{\partial_N\mathcal{B}} \bar{f} \delta p dA = 0, \\ G_d(\mathbf{u}, \delta d) &= \int_{\mathcal{B}} \left[(2\psi_c d + 2(d - 1)\mathcal{H}) \delta d + 2\psi_c l^2 \nabla d \cdot \nabla \delta d \right] dV = 0. \end{aligned} \quad (28)$$

This set of equations describes the constitutive model fully. Next, we use (28) as a departure point for the global-local approach in Section 3.

3. Extension Towards Global-Local Formulations

In this section the above introduced system of equations for the coupled problem will be solved using the Global-Local (GL) method, that is rooted in the domain decomposition approach [34]. It represents an initial contribution to the use of the GL formulation at *large deformations* for solving fracture mechanics problems numerically. The main objective here is to introduce an adoption of the hydraulic phase-field fracture formulation in poroelastic media within legacy codes, specifically for industrial applications. To this end, the material body \mathcal{B} is decomposed into a global domain \mathcal{B}_G representing a poroelastic media and a local domain \mathcal{B}_L reflecting the hydraulic fracturing (fracking) region. The global domain $\mathcal{B}_G := \mathcal{B}_C \cup \mathcal{B}_f \cup \Gamma$ is further split into a complementary domain \mathcal{B}_C corresponds to the intact area, a fictitious domain \mathcal{B}_f depicts a coarse projection of the local domain into the global one and an interface Γ between the unfractured and the fractured domains. The fictitious domain \mathcal{B}_f is a prolongation of \mathcal{B}_C towards \mathcal{B} , i.e. *recovering the space* of \mathcal{B} that is obtained by removing \mathcal{B}_L from its continuum domain, see Fig. 2. This gives the same constitutive modeling used in \mathcal{B}_C for \mathcal{B}_f . We also use the identical discretization space for both \mathcal{B}_f and \mathcal{B}_C , which results in $h_f := h_C$. The external loads are applied on \mathcal{B}_C and hence \mathcal{B}_L is assumed to be free from external loads. Such assumption is standard for the multi-scale setting, see [26].

At the interface Γ , global and local interfaces denoted as $\Gamma_G \subset \mathcal{B}_G$ and $\Gamma_L \subset \mathcal{B}_L$ are defined, such that in the continuum setting we have $\Gamma = \Gamma_G = \Gamma_L$. Hence, the deformation map $\boldsymbol{\varphi}$ and the fluid pressure p for both global and local domains do exactly coincide in the strong sense at interface, yielding

$$\boldsymbol{\varphi}_L(\mathbf{X}, t) \stackrel{!}{=} \boldsymbol{\varphi}_G(\mathbf{X}, t) \quad \text{and} \quad p_L(\mathbf{X}, t) \stackrel{!}{=} p_G(\mathbf{X}, t) \quad \text{at} \quad \mathbf{X} \in \Gamma. \quad (29)$$

However in a discrete setting we might have $\Gamma \neq \Gamma_G \neq \Gamma_L$ due to the presence of different meshing schemes (i.e. different element size/type used in \mathcal{B}_G and \mathcal{B}_L such that $h \neq h_L \neq h_G$ on Γ).

Remark 3.1. *The strong deformation/pressure continuity requirement given in Eq. 29 is too restrictive from the computational standpoint [25]. To resolve the phase field problem, one requires $h_L \ll h_G$. However, if we assume $\boldsymbol{\varphi}_L \stackrel{!}{=} \boldsymbol{\varphi}_G$ and $p_L \stackrel{!}{=} p_G$ on Γ , this yields $\Gamma_L = \Gamma_G$ in a discretized setting hence $h_L = h_G$ on Γ which contradicts $h_L \ll h_G$.*

Formulation 3.1 (Continuity conditions at interface). *Following Remark 3.1, we modify Eq. 29 in a strong sense by introducing the deformation $\boldsymbol{\varphi}_\Gamma(\mathbf{X}, t)$ and pressure $p_\Gamma(\mathbf{X}, t)$ interface and their corresponding traction forces $\{\boldsymbol{\lambda}_L^\varphi, \boldsymbol{\lambda}_C^\varphi\}$ and $\{\boldsymbol{\lambda}_L^p, \boldsymbol{\lambda}_C^p\}$ that are introduced as Lagrange multipliers. This results in a set of equations at the interface as*

$$\left\{ \begin{array}{ll} \boldsymbol{\varphi}_L(\mathbf{X}, t) = \boldsymbol{\varphi}_\Gamma(\mathbf{X}, t) & \text{at } \mathbf{X} \in \Gamma_L, \\ \boldsymbol{\varphi}_G(\mathbf{X}, t) = \boldsymbol{\varphi}_\Gamma(\mathbf{X}, t) & \text{at } \mathbf{X} \in \Gamma_G, \\ \boldsymbol{\lambda}_L^\varphi(\mathbf{X}, t) + \boldsymbol{\lambda}_C^\varphi(\mathbf{X}, t) = \mathbf{0} & \text{at } \mathbf{X} \in \Gamma, \end{array} \right. \quad \text{and} \quad \left\{ \begin{array}{ll} p_L(\mathbf{X}, t) = p_\Gamma(\mathbf{X}, t) & \text{at } \mathbf{X} \in \Gamma_L, \\ p_G(\mathbf{X}, t) = p_\Gamma(\mathbf{X}, t) & \text{at } \mathbf{X} \in \Gamma_G, \\ \boldsymbol{\lambda}_L^p(\mathbf{X}, t) + \boldsymbol{\lambda}_C^p(\mathbf{X}, t) = \mathbf{0} & \text{at } \mathbf{X} \in \Gamma. \end{array} \right.$$

Accordingly, the *single-scale* deformation map $\boldsymbol{\varphi}(\mathbf{X}, t)$ and fluid pressure field $p(\mathbf{X}, t)$

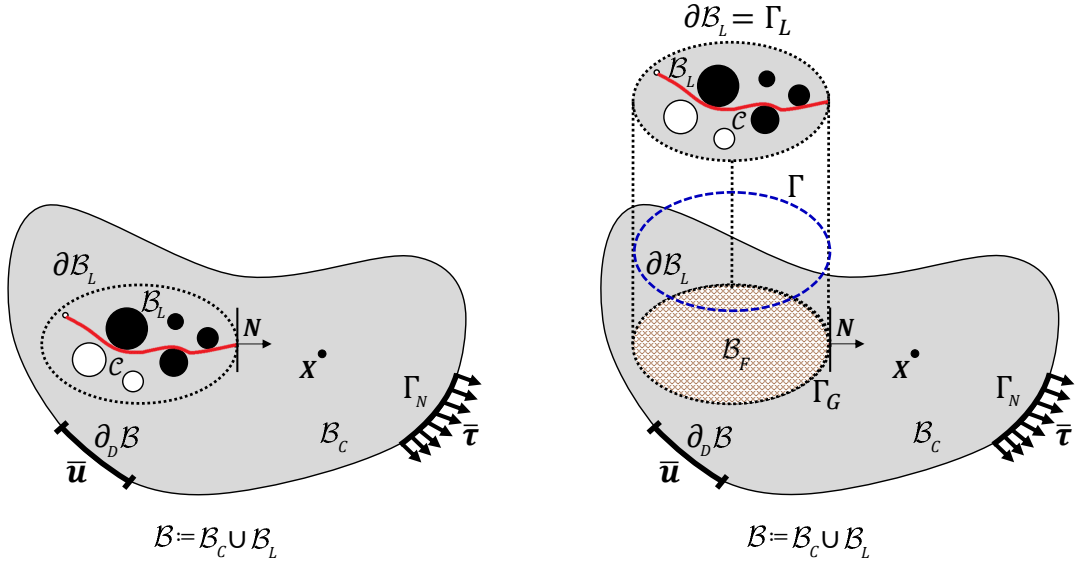


Figure 2: Illustration of the Global-Local formulation. (a) Geometry and loading setup of the single-scale boundary value problem. (b) Global-Local setting, by introduction of the fictitious domain \mathcal{B}_F through prolongation of \mathcal{B}_C to the entire domain whereas its unification is so-called global domain $\mathcal{B}_G := \mathcal{B}_C \cup \Gamma \cup \mathcal{B}_F$.

in Section 2 are decomposed as follows

$$\varphi(\mathbf{X}, t) = \begin{cases} \varphi_L(\mathbf{X}, t) & \text{for } \mathbf{X} \in \mathcal{B}_L, \\ \varphi_G(\mathbf{X}, t) & \text{for } \mathbf{X} \in \mathcal{B}_G, \\ \varphi_\Gamma(\mathbf{X}, t) & \text{for } \mathbf{X} \in \Gamma, \end{cases} \quad \text{and} \quad p(\mathbf{X}, t) = \begin{cases} p_L(\mathbf{X}, t) & \text{for } \mathbf{X} \in \mathcal{B}_L, \\ p_G(\mathbf{X}, t) & \text{for } \mathbf{X} \in \mathcal{B}_G, \\ p_\Gamma(\mathbf{X}, t) & \text{for } \mathbf{X} \in \Gamma. \end{cases} \quad (30)$$

The fracture surface lives only in \mathcal{B}_L . Hence we can introduce scalar-valued function $d_L(\mathbf{X}, t) : \mathcal{B}_L \rightarrow [0, 1]$. The *single-scale phase-field* d is then decomposed in the following representation

$$d(\mathbf{X}, t) := \begin{cases} d_L & \text{for } \mathbf{X} \in \mathcal{B}_L, \\ 0 & \text{for } \mathbf{X} \in \mathcal{B}_G. \end{cases} \quad (31)$$

Now the multi-physics problem for the Global-Local approach is based on eleven primary fields to characterize the hydro-poro-elasticity of fluid-saturated porous media at finite strains as

$$\text{Extended Primary Fields : } \mathfrak{P} := \{\varphi_G, \varphi_L, p_G, p_L, d_L, \boldsymbol{\lambda}_C^\varphi, \boldsymbol{\lambda}_L^\varphi, \lambda_C^p, \lambda_L^p, \varphi_\Gamma, p_\Gamma\}. \quad (32)$$

3.1. Governing formulations for the Global-Local coupling system

Based on the above introduced decompositions and the weak formulations outlined in (28), this section describes the GL weak forms of the PDEs for the coupled problem. The

global weak formulations of the deformation and pressure field take the form

$$\begin{aligned}
G_{\varphi_G}(\mathfrak{P}, \delta\varphi_G) &:= \int_{\mathcal{B}_G} \mathbf{P}(\nabla\varphi_G, p_G, 0) : \nabla\delta\varphi_G dV - \int_{\mathcal{B}_f} \mathbf{P}(\nabla\varphi_G, p_G, 0) : \nabla\delta\varphi_G dV \\
&\quad - \int_{\Gamma_G} \lambda_C^\varphi \cdot \delta\varphi_G dA - \int_{\Gamma_{N,G}} \bar{\tau} \cdot \delta\varphi_G dA = 0, \\
G_{p_G}(\mathfrak{P}, \delta p_G) &:= \int_{\mathcal{B}_G} \left[\frac{1}{M}(p_G - p_{G,n}) + B \left(J(\nabla\varphi_G) - J_n(\nabla\varphi_G) \right) \right] \delta p_G dV \\
&\quad + \int_{\mathcal{B}_G} \left[(\Delta t \mathbf{K}(\nabla\varphi_G, 0) \nabla p_G) \cdot \nabla \delta p_G \right] dV \\
&\quad + \int_{\mathcal{B}_f} \left[\frac{1}{M}(p_G - p_{G,n}) + B \left(J(\nabla\varphi_G) - J_n(\nabla\varphi_G) \right) - \Delta t \bar{r}_F \right] \delta p_G dV \\
&\quad + \int_{\mathcal{B}_f} \left[(\Delta t \mathbf{K}(\nabla\varphi_G, 0) \nabla p_G) \cdot \nabla \delta p_G \right] dV \\
&\quad - \int_{\Gamma_G} \lambda_C^p \delta p_G dA + \int_{\Gamma_{N,G}} \bar{f} \delta p_G dA = 0,
\end{aligned} \tag{G}$$

where $\delta\varphi_G \in \{\mathbf{H}^1(\mathcal{B}_G)^\delta : \delta\varphi_G = \mathbf{0} \text{ on } \partial_D \mathcal{B}\}$ and $\delta p_G \in \{H^1(\mathcal{B}_G) : \delta p_G = 0 \text{ on } \partial_D \mathcal{B}\}$ are the global test functions. Note that the pressure injection process of hydraulic fracturing \bar{r}_F exists only in the fictitious domain \mathcal{B}_f . The local weak formulations assumes the form

$$\begin{aligned}
G_{\varphi_L}(\mathfrak{P}, \delta\varphi_L) &:= \int_{\mathcal{B}_L} \mathbf{P}(\nabla\varphi_L, p_L, d_L) : \nabla\delta\varphi_L dV - \int_{\Gamma_L} \lambda_L^\varphi \cdot \delta\varphi_L dA = 0, \\
G_{p_L}(\mathfrak{P}, \delta p_L) &:= \int_{\mathcal{B}_L} \left[\frac{1}{M}(p_L - p_{L,n}) + B \left(J(\nabla\varphi_L) - J_n(\nabla\varphi_L) \right) \right] \delta p_L dV \\
&\quad + \int_{\mathcal{B}_L} \left[(\Delta t \mathbf{K}(\nabla\varphi_L, d_L) \nabla p_L) \cdot \nabla \delta p_L \right] dV - \int_{\Gamma_L} \lambda_L^p \delta p_L dA = 0 \\
G_{d_L}(\mathfrak{P}, \delta d_L) &:= \int_{\mathcal{B}_L} \left[(2\psi_c d_L + 2(d_L - 1) \mathcal{H}(\nabla\varphi_L)) \delta d_L + 2\psi_c l^2 \nabla d_L \cdot \nabla \delta d_L \right] dV = 0,
\end{aligned} \tag{L}$$

where $\delta\varphi_L \in \mathbf{H}^1(\mathcal{B}_L)$, $\delta p_L \in H^1(\mathcal{B}_L)$ and $\delta d_L \in H^1(\mathcal{B}_L)$ are the local test functions for the deformation, fluid pressure and crack phase-field, respectively.

Next, we derive the weak formulations for the deformation and pressure continuity at interface Γ introduced in Formulation 3.1 by using a standard Galerkin procedure

$$G_{\varphi_\Gamma}(\mathfrak{P}, \delta\varphi_\Gamma) := \int_{\Gamma} (\lambda_C^\varphi + \lambda_L^\varphi) \cdot \delta\varphi_\Gamma dA = 0, \tag{C_1}$$

$$G_{\lambda_C^\varphi}(\mathfrak{P}, \delta\lambda_C^\varphi) := \int_{\Gamma} (\varphi_\Gamma - \varphi_G) \cdot \delta\lambda_C^\varphi dA = 0, \tag{C_2}$$

$$G_{\lambda_L^\varphi}(\mathfrak{P}, \delta\lambda_L^\varphi) := \int_{\Gamma} (\varphi_\Gamma - \varphi_L) \cdot \delta\lambda_L^\varphi dA = 0, \tag{C_3}$$

$$G_{p_\Gamma}(\mathfrak{P}, \delta p_\Gamma) := \int_{\Gamma} (\lambda_C^p + \lambda_L^p) \delta p_\Gamma dA = 0, \tag{C_4}$$

$$G_{\lambda_C^p}(\mathfrak{P}, \delta\lambda_C^p) := \int_{\Gamma} (p_\Gamma - p_G) \delta\lambda_C^p dA = 0, \tag{C_5}$$

$$G_{\lambda_L^p}(\mathfrak{P}, \delta\lambda_L^p) := \int_{\Gamma} (p_{\Gamma} - p_L) \delta\lambda_L^p dA = 0, \quad (C_6)$$

herein $\delta\varphi_{\Gamma} \in \mathbf{H}^1(\Gamma)$; $\delta p_{\Gamma} \in H^1(\Gamma)$; $\delta\lambda_C^{\varphi}, \delta\lambda_L^{\varphi} \in \mathbf{L}^2(\Gamma)$ and $\delta\lambda_C^p, \delta\lambda_L^p \in L^2(\Gamma)$ are the corresponding test functions. Equations (G), (L) and (C1)–(C6) specify the entire system of the Global-Local approach.

3.2. Dirichlet-Neumann type boundary conditions

Within a Global-Local computational scheme, instead of finding the stationary solution of the (G), (L) along with (C1) – (C6) in the monolithic sense, an alternate minimization is employed. This is in line with [30], which leads to the Global-Local formulation using the concept of non-intrusiveness. Here the global and local level are solved in a multiplicative manner according to the idea of Schwarz' alternating method [53].

Let $k \geq 0$ be the Global-Local iteration index at a fixed loading step n . The iterative solution procedure for the Global-Local computational scheme is as follows:

- Dirichlet local problem: solution of local problem (L) coupled with (C3) and (C6),
- Pre-processing global level: recovery phase using (C1) and (C4),
- Neumann global problem: solution of global problem (G),
- Post-processing global level: recovery phase using (C2) and (C5).

Despite of its strong non-intrusiveness [28], there are two shortcomings embedded in the system which have to be resolved. (a) Due to the extreme difference in stiffness between the local domain and its projection to the global level, i.e. fictitious domain \mathcal{B}_f , a relaxation/acceleration techniques has to be used, see [30]. (b) Additionally, it turns out that if the solution vector

$$\mathfrak{P}^k = (\varphi_G^k, \varphi_L^k, p_G^k, p_L^k, d_L^k, \lambda_C^{\varphi,k}, \lambda_L^{\varphi,k}, \lambda_C^{p,k}, \lambda_L^{p,k}, \varphi_{\Gamma}^k, p_{\Gamma}^k) \quad (33)$$

is plugged into equations (G), (L), (C1) – (C6), the imbalanced quantities for the deformation and pressure fields follow

$$\int_{\Gamma} (\varphi_{\Gamma}^k - \varphi_L^k) \cdot \delta\lambda_L^{\varphi} dA \neq 0 \quad \text{and} \quad \int_{\Gamma} (p_{\Gamma}^k - p_L^k) \delta\lambda_L^p dA \neq 0, \quad (34)$$

resulting in the *iterative* Global-Local computation scheme. The aforementioned difficulties motivate us to provide alternative coupling conditions that overcome these challenges, which are explained in the following section.

3.3. Robin-type boundary conditions

In this section, the Global-Local formulation is enhanced using Robin-type boundary conditions to relax the stiff local response that is observed at the global level (due to the local non-linearity). Furthermore the computational time is reduced. This improves the resolution of the imbalanced quantities in (34) and it accelerates Global-Local computational iterations.

Recall, the coupling equations denoted in (C1) – (C6) arise from the continuity conditions at the interface in a strong sense. That provides the boundary conditions which have to be imposed on the global and local levels. At that level the Robin-type boundary conditions are formulated.

3.3.1. Robin-type boundary conditions at the local level.

Finite deformation. For the mechanical deformation field at the local level, a new coupling term is introduced as a combination of (C₁) and (C₂)

$$G_{\varphi_\Gamma}(\mathfrak{P}, \delta\varphi_\Gamma) + \mathbb{A}_L^\varphi G_{\lambda_C^\varphi}(\mathfrak{P}, \delta\lambda_C^\varphi) = \int_\Gamma (\lambda_C^\varphi + \lambda_L^\varphi) \cdot \delta\varphi_\Gamma dA + \mathbb{A}_L^\varphi \int_\Gamma (\varphi_\Gamma - \varphi_G) \cdot \delta\lambda_C^\varphi dA = 0 \quad (35)$$

This leads for iteration k to

$$\int_\Gamma (\lambda_C^{\varphi, k-1} + \lambda_L^{\varphi, k}) \cdot \delta\varphi_\Gamma dA + \mathbb{A}_L^\varphi \int_\Gamma (\varphi_\Gamma^{k, \frac{1}{2}} - \varphi_G^{k-1}) \cdot \delta\lambda_C^\varphi dA = 0. \quad (36)$$

Herein, \mathbb{A}_L^φ is a local augmented stiffness matrix for the deformation applied at the interface which serves as regularization of the local Jacobian matrix. By means of (36) at iteration k , the local system of equations for the mechanical problem at the interface (C₁) – (C₃) results in the following modified boundary conditions

$$\int_\Gamma \lambda_L^{\varphi, k} \cdot \delta\varphi_\Gamma dA + \mathbb{A}_L^\varphi \int_\Gamma \varphi_\Gamma^{k, \frac{1}{2}} \cdot \delta\lambda_C^\varphi dA = \Lambda_L^{\varphi, k-1}, \quad (\tilde{C}_1)$$

$$\int_\Gamma (\varphi_\Gamma^{k, \frac{1}{2}} - \varphi_L^k) \cdot \delta\lambda_L^\varphi dA = 0, \quad (\tilde{C}_2)$$

with

$$\Lambda_L^{\varphi, k-1} := \Lambda_L(\lambda_C^{\varphi, k-1}, \varphi_G^{k-1}; \mathbb{A}_L^\varphi) = \mathbb{A}_L^\varphi \int_\Gamma \varphi_G^{k-1} \cdot \delta\lambda_C^\varphi dA - \int_\Gamma \lambda_C^{\varphi, k-1} \cdot \delta\varphi_\Gamma dA. \quad (37)$$

Fluid pressure. Analogously to the coupling terms for the deformation introduced above, we modify the local system of equations for the pressure field at the interface (C₄) – (C₆). It results in the following modified boundary conditions

$$\int_\Gamma \lambda_L^{p, k} \delta p_\Gamma dA + \mathbb{A}_L^p \int_\Gamma p_\Gamma^{k, \frac{1}{2}} \delta \lambda_C^p dA = \Lambda_L^{p, k-1}, \quad (\tilde{C}_3)$$

$$\int_\Gamma (p_\Gamma^{k, \frac{1}{2}} - p_L^k) \delta \lambda_L^p dA = 0, \quad (\tilde{C}_4)$$

with

$$\Lambda_L^{p, k-1} := \Lambda_L(\lambda_C^{p, k-1}, p_G^{k-1}; \mathbb{A}_L^p) = \mathbb{A}_L^p \int_\Gamma p_G^{k-1} \delta \lambda_C^p dA - \int_\Gamma \lambda_C^{p, k-1} \delta p_\Gamma dA. \quad (38)$$

Along with (L), the local system of equations has to be solved for $(\varphi_L^k, p_L^k, \lambda_L^{\varphi, k}, \lambda_L^{p, k}, \varphi_\Gamma^{k, \frac{1}{2}}, p_\Gamma^{k, \frac{1}{2}})$ for given local Robin-type parameters $(\Lambda_L^{\varphi, k-1}, \Lambda_L^{p, k-1}, \mathbb{A}_L^\varphi, \mathbb{A}_L^p)$.

Remark 3.2. In the numerical implementation, the current local fields are computed based on the old global variables as history fields, see (36). Hereby, the deformation φ_Γ and fluid pressure p_Γ at the interface are updated at iteration $(k, \frac{1}{2})$. This choice is essential for the construction of the Robin-type boundary conditions. Note that, we proved in previous work that $\mathbf{u}_\Gamma^{(k, \frac{1}{2})} = \mathbf{u}_\Gamma^k$ with $\varphi := \mathbf{u} + \mathbf{X}$ where \mathbf{X} is a fixed initial configuration, see [54]. With this prove at interface the continuity conditions are satisfied yielding a well posed problem and accelerate the convergence results. Note that other coupling conditions at the interface, i.e. updating the deformation and pressure at iteration k in (\tilde{C}_2) and (\tilde{C}_4) gives ill-posed problem due to the imposition of both Neumann and Dirichlet boundary conditions at same time at Γ .

3.3.2. Robin-type boundary conditions at the global level.

Finite deformation. Accordingly, at the global level, the new coupling term is stated as a combination of (C_1) and (C_3) for the mechanical deformation as

$$G_{\varphi_\Gamma}(\mathfrak{P}, \delta\varphi_\Gamma) + \mathbb{A}_G^\varphi G_{\lambda_L^\varphi}(\mathfrak{P}, \delta\lambda_L^\varphi) = \int_\Gamma (\lambda_C^\varphi + \lambda_L^\varphi) \cdot \delta\varphi_\Gamma dA + \mathbb{A}_G^\varphi \int_\Gamma (\varphi_\Gamma - \varphi_L) \cdot \delta\lambda_L^\varphi dA = 0 \quad (39)$$

This leads for iteration k to

$$\int_\Gamma (\lambda_C^{\varphi,k} + \lambda_L^{\varphi,k}) \cdot \delta\varphi_\Gamma dA + \mathbb{A}_G^\varphi \int_\Gamma (\varphi_\Gamma^k - \varphi_L^k) \cdot \delta\lambda_L^\varphi dA = 0, \quad (40)$$

where, \mathbb{A}_G^φ is a global augmented stiffness matrix for the deformation applied on the interface. Through (40) at the iteration k , the Robin-type boundary condition at the global level follows

$$\int_\Gamma \lambda_C^{\varphi,k} \cdot \delta\varphi_\Gamma dA + \mathbb{A}_G^\varphi \int_\Gamma \varphi_\Gamma^k \cdot \delta\lambda_L^\varphi dA = \Lambda_G^{\varphi,k}, \quad (\tilde{C}_5)$$

$$\int_\Gamma (\varphi_\Gamma^{k,\frac{1}{2}} - \varphi_G^k) \cdot \delta\lambda_C^\varphi dA = 0, \quad (\tilde{C}_6)$$

with

$$\Lambda_G^{\varphi,k} := \Lambda_G(\lambda_L^{\varphi,k}, \varphi_L^k; \mathbb{A}_G^\varphi) = \mathbb{A}_G^\varphi \int_\Gamma \varphi_L^k \cdot \delta\lambda_L^\varphi dA - \int_\Gamma \lambda_L^{\varphi,k} \cdot \delta\varphi_\Gamma dA. \quad (41)$$

Fluid pressure. Following the same procedure as above, the Robin-type boundary condition at the global level for the pressure field yields

$$\int_\Gamma \lambda_C^{p,k} \delta p_\Gamma dA + \mathbb{A}_G^p \int_\Gamma p_\Gamma^k \delta\lambda_L^p dA = \Lambda_G^{p,k}, \quad (\tilde{C}_7)$$

$$\int_\Gamma (p_\Gamma^{k,\frac{1}{2}} - p_G^k) \delta\lambda_C^p dA = 0, \quad (\tilde{C}_8)$$

with

$$\Lambda_G^{p,k} := \Lambda_L(\lambda_L^{p,k}, p_L^k; \mathbb{A}_G^p) = \mathbb{A}_G^p \int_\Gamma p_L^k \delta\lambda_L^p dA - \int_\Gamma \lambda_L^{p,k} \delta p_\Gamma dA. \quad (42)$$

Together with (G), the global system of equations has to be solved for $(\varphi_G^k, p_G^k, \lambda_C^{\varphi,k}, \lambda_C^{p,k}, \varphi_\Gamma^k, p_\Gamma^k)$ for a given $(\Lambda_G^{\varphi,k}, \Lambda_G^{p,k}, \mathbb{A}_G^\varphi, \mathbb{A}_G^p, \varphi_\Gamma^{k,\frac{1}{2}}, p_\Gamma^{k,\frac{1}{2}})$. Here, $(\mathbb{A}_G^\varphi, \mathbb{A}_G^p, \Lambda_G^{\varphi,k}, \Lambda_G^{p,k})$ stand for global Robin-type parameters.

Based on the new boundary conditions provided in $(\tilde{C}_1) - (\tilde{C}_8)$ the imbalanced quantities in the Global-Local iterations read

$$\int_\Gamma (\varphi_\Gamma^k - \varphi_\Gamma^{k,\frac{1}{2}}) \cdot \delta\lambda_L^\varphi dA \neq 0 \quad \text{and} \quad \int_\Gamma (p_\Gamma^k - p_\Gamma^{k,\frac{1}{2}}) \delta\lambda_L^p dA \neq 0 \quad (43)$$

For the specific Robin-type boundary conditions, we can resolve (43) such that this term does not produce any error in the iterative procedure. To do so, following our previous

work [54], the global and local augmented stiffness matrices for both, the deformation and pressure fields, within the Robin-type boundary conditions are given by

$$\mathbb{A}_G = \mathbf{L}_L^T \mathbf{T}_L^{-T} \mathbf{S}_L \quad \text{and} \quad \mathbb{A}_L := \mathbf{S}_C. \quad (44)$$

\mathbb{A}_G and \mathbb{A}_L can be seen as augmented stiffness matrices regularize the Jacobian stiffness matrix at the global and local levels, respectively. For details on the derivation of those matrices, we refer the interested reader to [54].

Remark 3.3. *Note that the choice of the coupling equations $(C_1) - (C_6)$ at the local and global level for the Robin-type boundary conditions are the outcome of precise investigation of different combinations. However other choices are also possible, but one needs to adapt/derive the imbalance equations in (43) accordingly.*

The detailed Global-Local formulation using Robin-type boundary conditions is depicted in Algorithm 1. The Global-Local setting provides a generic two-scale finite element algorithms that enables capturing local non-linearities.

3.4. Predictor-Corrector mesh adaptivity

The Global-Local approach is augmented by a *dynamic allocation* of a local state using an adaptive scheme which has to be performed at time step t_n in Algorithm 1. By

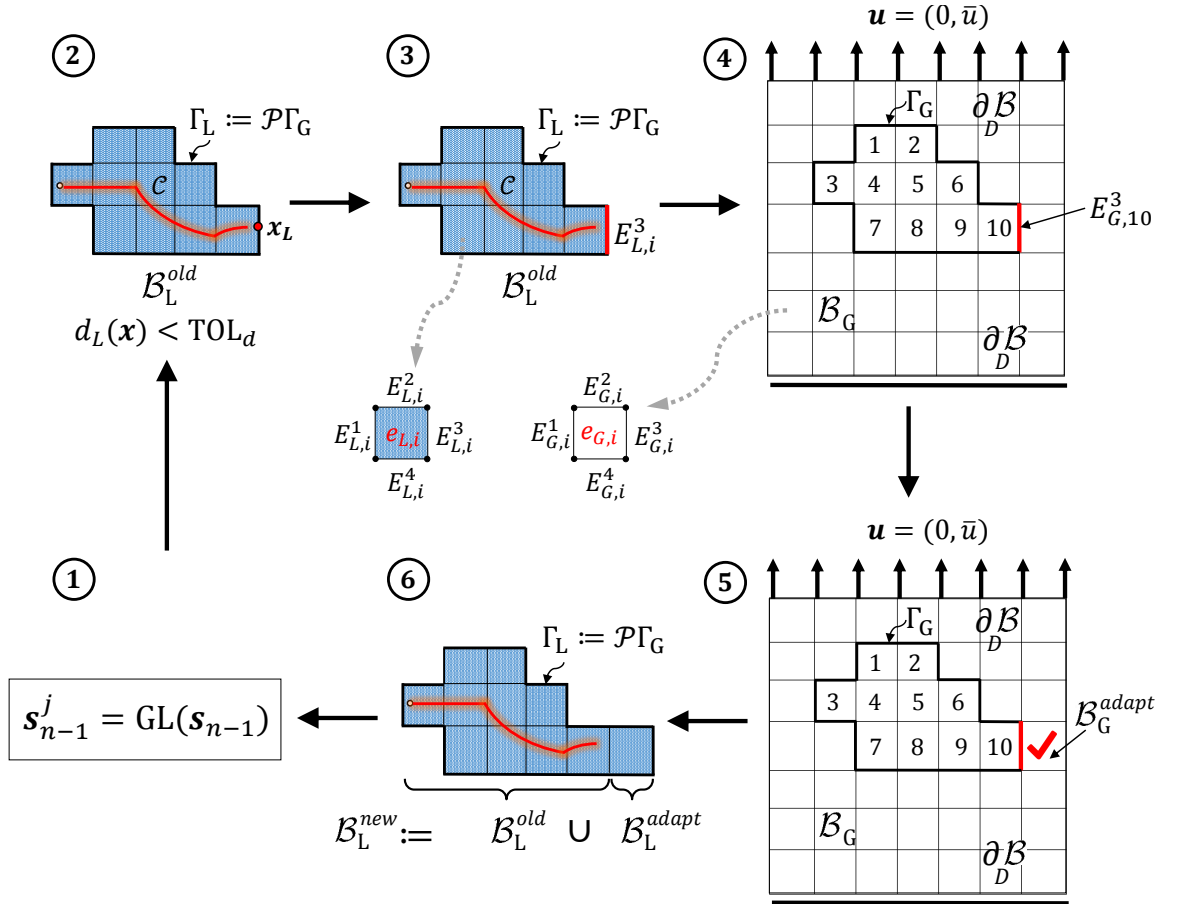


Figure 3: Explanation of the predictor-corrector adaptive scheme, introduced in [54].

the adaptivity procedure, we mean: (a) to determine which global elements need to be refined; (b) to create the new fictitious and local domain, see Fig. 3; (c) to determine a new local interface; (d) to interpolate the old global solution. For details regarding the predictor-corrector adaptive scheme applied to the global-local formulation, we refer the interested reader to [37, 54] and Algorithm 2-3 therein.

Algorithm 1 *Global-Local iterative scheme combined with Robin-type boundary conditions.*

Input: loading data $(\bar{\varphi}_n, \bar{p}_n)$ on $\partial_D \mathcal{B}$;

solution $\mathfrak{P}_{n-1} := (\varphi_{G,n-1}, p_{G,n-1}, \varphi_{L,n-1}, p_{L,n-1}, d_{L,n-1}, \varphi_{\Gamma,n-1}, p_{\Gamma,n-1}, \lambda_{C,n-1}^\varphi, \lambda_{L,n-1}^\varphi, \lambda_{C,n-1}^p, \lambda_{L,n-1}^p)$ and $\mathcal{H}_{L,n-1}$ from step $n-1$.

Global-Local iteration $k \geq 1$:

Local boundary value problem:

- given $\mathcal{A}_L^\varphi, \mathcal{A}_L^p, \Lambda_L^{\varphi,k-1}, \Lambda_L^{p,k-1}, \mathcal{H}_{L,n-1}$; solve
 phase-field part: $\int_{\mathcal{B}_L} \left[(2\psi_c d_L + 2(d_L - 1) \mathcal{H}(\nabla \varphi_L)) \delta d_L + 2\psi_c l^2 \nabla d_L \cdot \nabla \delta d_L \right] dV = 0$,
 mechanical part:

$$\begin{cases} \int_{\mathcal{B}_L} \mathbf{P}(\nabla \varphi_L, p_L, d_L) : \nabla \delta \varphi_L dV - \int_{\Gamma_L} \lambda_L^\varphi \cdot \delta \varphi_G dA = 0, \\ \int_{\Gamma} \lambda_L^\varphi \cdot \delta \varphi_\Gamma dA + \mathcal{A}_L^\varphi \int_{\Gamma} \varphi_\Gamma \cdot \delta \lambda_C^\varphi dA = \Lambda_L^{\varphi,k-1} \quad \text{and} \quad \int_{\Gamma} (\varphi_\Gamma - \varphi_L) \cdot \delta \lambda_L^\varphi dA = 0, \end{cases}$$

 fluid pressure:

$$\begin{cases} \int_{\mathcal{B}_L} \left[\frac{1}{M} (p_L - p_{L,n}) + B(J(\nabla \varphi_L) - J_n(\nabla \varphi_L)) \right] \delta p_L dV \\ + \int_{\mathcal{B}_L} \left[(\Delta t \mathbf{K}(\nabla \varphi_L, d_L) \nabla p_L) \cdot \nabla \delta p_L \right] dV - \int_{\Gamma_L} \lambda_L^p \delta p_L dA = 0, \\ \int_{\Gamma} \lambda_L^p \delta p_\Gamma dA + \mathcal{A}_L^p \int_{\Gamma} p_\Gamma \delta \lambda_C^p dA = \Lambda_L^{p,k-1} \quad \text{and} \quad \int_{\Gamma} (p_\Gamma - p_L) \delta \lambda_L^p dA = 0, \end{cases}$$

 set $(\varphi_L, p_L, d_L, \varphi_\Gamma, p_\Gamma, \lambda_L^\varphi, \lambda_L^p) := (\varphi_L^k, p_L^k, d_L^k, \varphi_\Gamma^{k, \frac{1}{2}}, p_\Gamma^{k, \frac{1}{2}}, \lambda_L^{\varphi,k}, \lambda_L^{p,k})$,
 • given $(\varphi_L^k, p_L^k, \lambda_L^{\varphi,k}, \lambda_L^{p,k}; \mathcal{A}_G^\varphi, \mathcal{A}_G^p)$, set
 $\Lambda_G^{\varphi,k} = \mathcal{A}_G^\varphi \int_{\Gamma} \varphi_L^k \cdot \delta \lambda_C^\varphi dA - \int_{\Gamma} \lambda_L^{\varphi,k} \cdot \delta \varphi_\Gamma dA$; $\Lambda_G^{p,k} = \mathcal{A}_G^p \int_{\Gamma} p_L^k \delta \lambda_C^p dA - \int_{\Gamma} \lambda_L^{p,k} \delta p_\Gamma dA$.

Global boundary value problem:

- given $\mathcal{A}_G^\varphi, \mathcal{A}_G^p, \Lambda_G^{\varphi,k}, \Lambda_G^{p,k}, \varphi_\Gamma^{k, \frac{1}{2}}, p_\Gamma^{k, \frac{1}{2}}$, solve
 mechanical part:

$$\begin{cases} \int_{\mathcal{B}_G} \mathbf{P}(\nabla \varphi_G, p_G, 0) : \nabla \delta \varphi_G dV - \int_{\mathcal{B}_f} \mathbf{P}(\nabla \varphi_G, p_G, 0) : \nabla \delta \varphi_G dV \\ - \int_{\Gamma} \lambda_C^\varphi \cdot \delta \varphi_G dA - \int_{\Gamma_N} \bar{\tau} \cdot \delta \varphi_G dA = 0, \\ \int_{\Gamma} \lambda_C^\varphi \cdot \delta \varphi_\Gamma dA + \mathcal{A}_G^\varphi \int_{\Gamma} \varphi_\Gamma \cdot \delta \lambda_L^\varphi dA = \Lambda_G^{\varphi,k} \quad \text{and} \quad \int_{\Gamma} (\varphi_\Gamma^{k, \frac{1}{2}} - \varphi_G) \cdot \delta \lambda_C^\varphi dA = 0, \end{cases}$$

 fluid pressure:

$$\begin{cases} \int_{\mathcal{B}_G} \left[\frac{1}{M} (p_G - p_{G,n}) + B(J(\nabla \varphi_G) - J_n(\nabla \varphi_G)) \right] \delta p_G dV - \int_{\Gamma} \lambda_C^p \delta p_G dA \\ + \int_{\mathcal{B}_G} \left[(\Delta t \mathbf{K}(\nabla \varphi_G) \nabla p_G) \cdot \nabla \delta p_G \right] dV + \int_{\mathcal{B}_f} \left[\frac{1}{M} (p_G - p_{G,n}) + B(J(\nabla \varphi_G) \right. \\ \left. - J_n(\nabla \varphi_G)) \right] \delta p_G dV + \int_{\mathcal{B}_f} \left[(\Delta t \mathbf{K}(\nabla \varphi_G) \nabla p_G) \cdot \nabla \delta p_G - \Delta t \bar{r}_F \right] dV + \int_{\Gamma_N} \bar{f} \delta p_G dA = 0, \\ \int_{\Gamma} \lambda_C^p \delta p_\Gamma dA + \mathcal{A}_G^p \int_{\Gamma} p_\Gamma \delta \lambda_L^p dA = \Lambda_G^{p,k} \quad \text{and} \quad \int_{\Gamma} (p_\Gamma^{k, \frac{1}{2}} - p_G) \delta \lambda_C^p dA = 0, \end{cases}$$

 set $(\varphi_G, p_G, \varphi_\Gamma, p_\Gamma, \lambda_C^\varphi, \lambda_C^p) := (\varphi_G^k, p_G^k, \varphi_\Gamma^k, p_\Gamma^k, \lambda_C^{\varphi,k}, \lambda_C^{p,k})$,
 • given $(\varphi_G^k, p_G^k, \lambda_C^{\varphi,k}, \lambda_C^{p,k}; \mathcal{A}_L^\varphi, \mathcal{A}_L^p)$, set
 $\Lambda_L^{\varphi,k} = \mathcal{A}_L^\varphi \int_{\Gamma} \varphi_G^k \cdot \delta \lambda_C^\varphi dA - \int_{\Gamma} \lambda_C^{\varphi,k} \cdot \delta \varphi_\Gamma dA$ and $\Lambda_L^{p,k} = \mathcal{A}_L^p \int_{\Gamma} p_G^k \delta \lambda_C^p dA - \int_{\Gamma} \lambda_C^{p,k} \delta p_\Gamma dA$.
 • if fulfilled, set $\mathfrak{P}^k =: \mathfrak{P}_n$ and stop;
 else $k+1 \rightarrow k$.

Output: solution \mathfrak{P}_n and $\mathcal{H}_{L,n}$.

Table 1: Material parameters used in the numerical examples based on [47, 70].

No.	Parameter	Name	Value	Unit
1.	E	Young's modulus	15.96	GPa
2.	ν	Poisson's ratio	0.2	–
3.	M	Biot's modulus	12.5	GPa
4.	B	Biot's coefficient	0.79	–
5.	K	Intrinsic permeability	2×10^{-14}	m^2
6.	K_c	Spatial permeability in fracture	83.3	$\text{m}^3\text{s/kg}$
7.	ζ	Permeability transition exponent	50	–
8.	η_F	Dynamic fluid viscosity	1×10^{-3}	$\text{kg}/(\text{m.s})$
9.	σ_c	Critical effective stress	0.005	GPa

4. Numerical Examples

This section demonstrates the performance of the proposed adaptive Global-Local approach applied to the phase-field modeling of hydraulic fracture in fluid-saturated porous media. Two numerical model problems for the GL formulations are investigated. A considerable reduction of the computational cost is observed in comparison with the single-scale solution. The material parameters used in both examples are listed in Table 1 and based on [47, 70]. For the numerical simulation all variables in both, the global and local domains, are discretized by bilinear quadrilateral $Q1$ finite elements. The total number of elements for the single-scale problem is 28900 elements and for Global domain is 100 elements. The number of elements for the local domain is determined based on predictor-corrector mesh adaptivity.

4.1. Hydraulically induced crack driven by fluid volume injection

In the first numerical example, a boundary value problem applied to the square plate is shown in Fig. 4. We set $A = 40 \text{ m}$ hence $\mathcal{B} = (0, 80)^2 \text{ m}^2$ that includes a predefined single notch \mathcal{C}_1 of length 8 m in the body center with $a = (36, 40)$ and $b = (44, 40)$, as

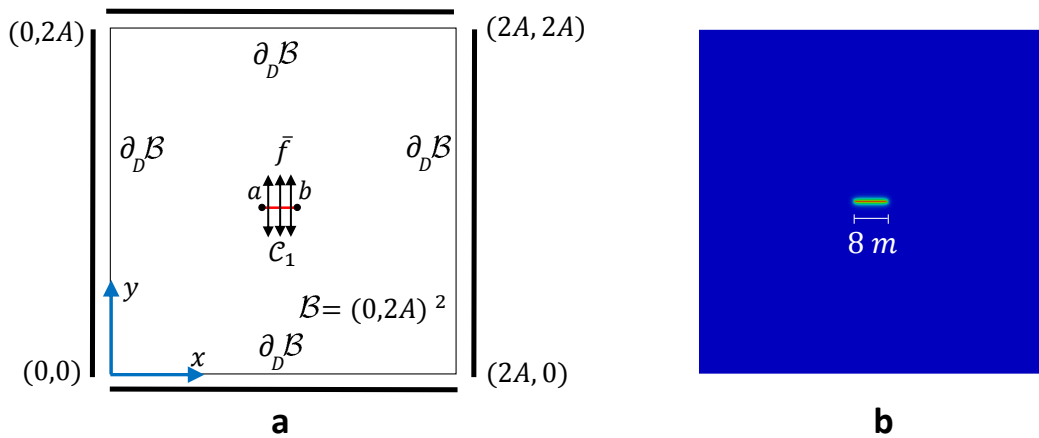


Figure 4: Hydraulically induced crack driven by fluid volume injection. (a) Geometry and boundary conditions and (b) described crack phase-field d as a Dirichlet boundary conditions at $t = 0 \text{ s}$.

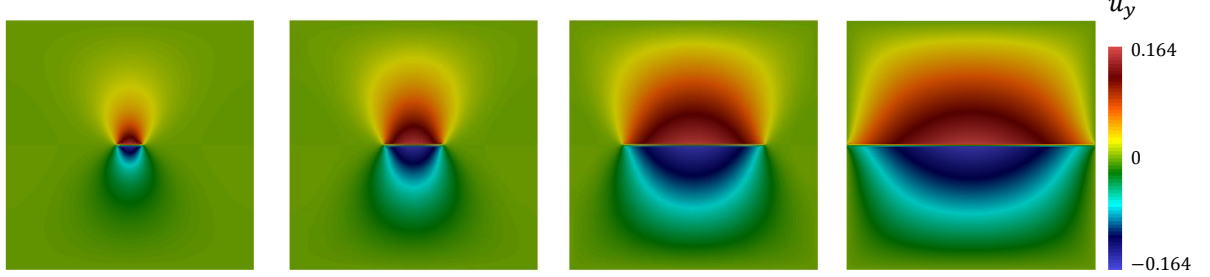
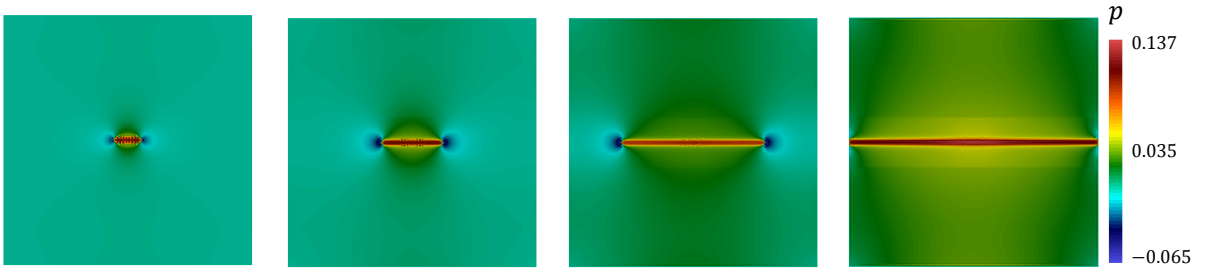
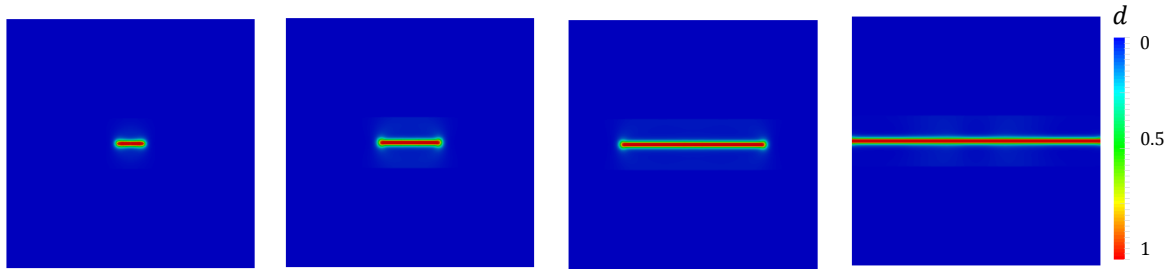
Single – scale vertical displacement**Single – scale pressure****Single – scale crack phase – field**

Figure 5: Example 1. Single-scale results of the hydraulically induced crack driven by fluid volume injection. Evolution of the vertical displacement u_y (first row), fluid pressure p (second row) and crack phase-field d (third row) for different deformation stages up to final failure at $[t = 1.8; 6.5; 20; 48.5 \text{ s}]$.

depicted in Fig. 4. A constant fluid flow of $\bar{f} = 0.002 \text{ m}^2/\text{s}$ is injected in \mathcal{C}_1 . At the boundary $\partial_D \mathcal{B}$, all the displacements are fixed in both directions and the fluid pressure is set to zero. Fluid injection \bar{f} continues until failure for $T = 49 \text{ s}$ with time step $\Delta t = 0.1 \text{ s}$ during the simulation.

We start our analysis by illustrating the single-scale results for different deformations states up to final failure. The vertical displacement u_y (first row), fluid pressure p (second row) and crack phase-field d (third row) evolutions are demonstrated in Figure 5 for four time steps $[t = 1.8; 6.5; 20; 48.5 \text{ s}]$. The crack initiates at the notch-tips due to fluid pressure increase until a threshold energy ψ_c is reached. Thereafter, the crack propagates horizontally in two direction towards the boundaries. In the fractured zone, p is almost constant due to the increased permeability inside the crack. Whereas, low fluid pressure in the surrounding is observed due the chosen small time-step in comparison with the

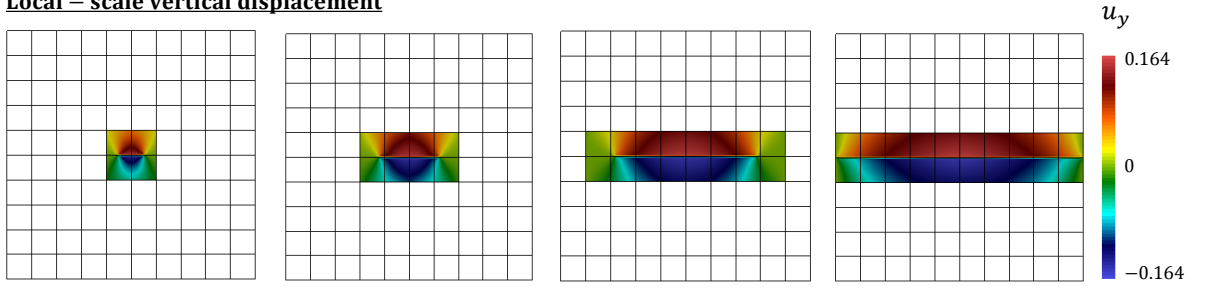
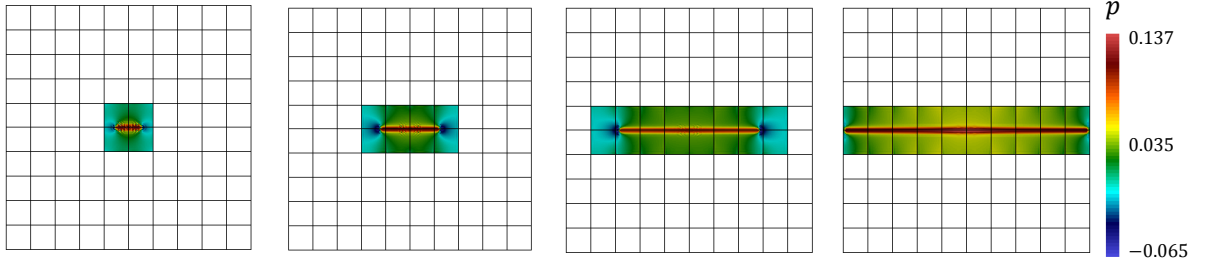
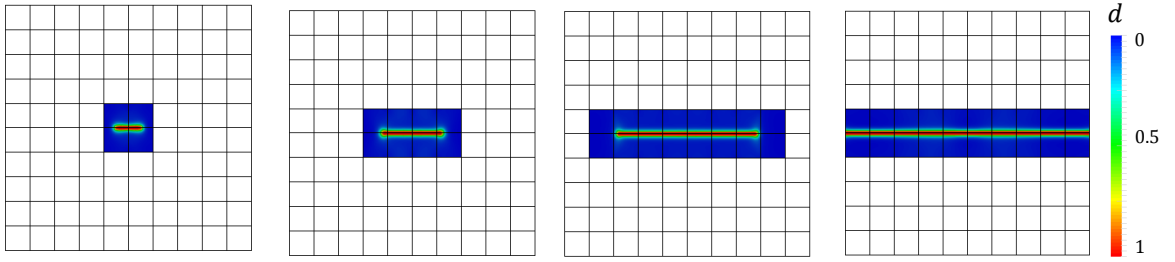
Local – scale vertical displacement**Local – scale pressure****Local – scale crack phase – field****Local – scale mesh evolution**

Figure 6: Example 1. Local-scale results of the hydraulically induced crack driven by fluid volume injection. Evolution of the vertical displacement u_y (first row), fluid pressure p (second row), crack phase-field d (third row) and local domain (fourth row) for different fluid injection time steps at $[t = 1.8; 6.5; 20; 48.5 \text{ s}]$ up to final failure.

permeability of the porous medium, as outlined in [47]. The fluid pressure drops down while the crack propagates further as shown in Figure 5 (second row, middle states). Then, p increases again due to the prescribed fixed boundary conditions $\partial_D \mathcal{B}$, see Fig. 5 (second row, last state).

Next the performance of the Global-Local approach is investigated. To this end, the evolution of the vertical displacement u_y (first row), fluid pressure p (second row), crack phase-field d (third row) and local domain (fourth row) for different fluid injection time steps $t = 1.8; 6.5; 20; 48.5 \text{ s}$ are demonstrated in Fig. 6 for the local-scale and in Fig. 7 for the homogenized global scale. Hereby, even with less number of elements at the global domain the overall response is qualitatively in a good agreement with the single-scale domain.

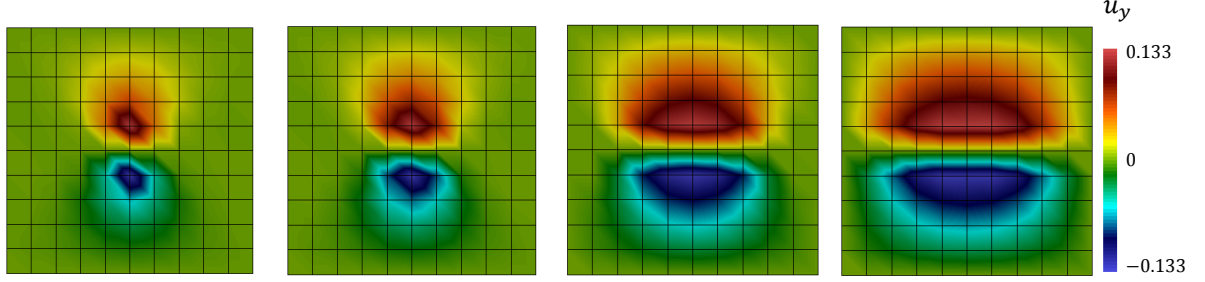
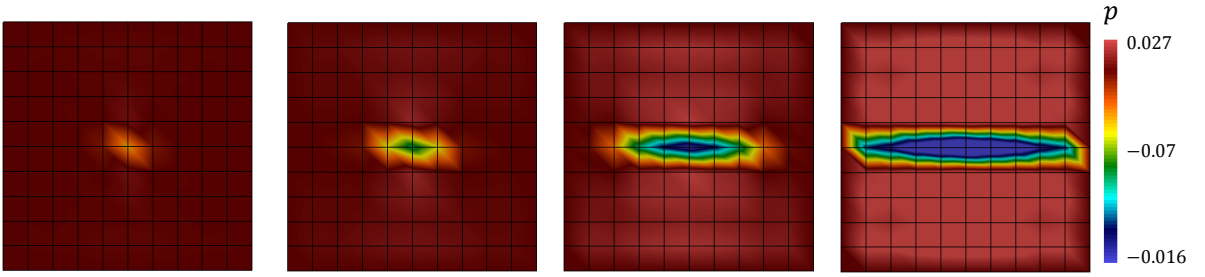
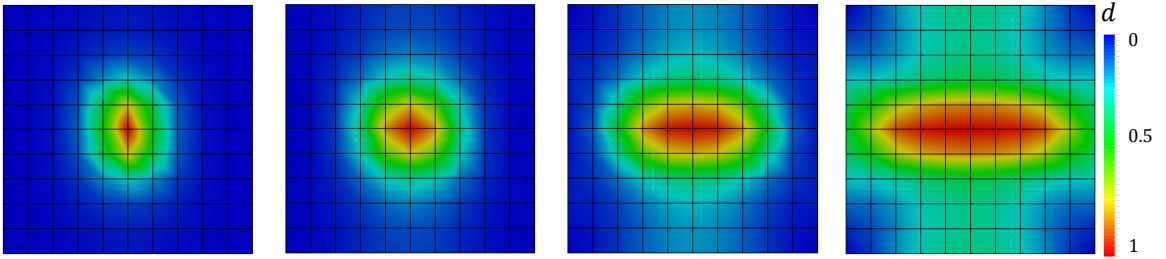
Global – scale vertical displacement**Global – scale pressure****Global – scale crack phase – field**

Figure 7: Example 1. Global-scale results of the hydraulically induced crack driven by fluid volume injection. Evolution of the vertical displacement u_y (first row), fluid pressure p (second row) and crack phase-field d (third row) for different deformation stages up to final failure at $t = 1.8; 6.5; 20; 48.5$ s.

Figure 8a describes the maximum injected fluid pressure within the crack region versus the fluid injection time. For a comparison purpose, the Global-Local and single-scale solutions are both provided. The results obtained from Global-Local formulation are in a good agreement with the single-scale solution. Furthermore, it is noted that the injected fluid pressure increases within the crack region before it reaches to the peak point. Thereafter, as expected a drop of the fluid pressure is observed.

To illustrate the efficiency of the predictor-corrector adaptive scheme, we plot in 8b the corresponding accumulative computational time and in Fig. 9a the total number of unknowns (local and global problems) versus the fluid injection time and compared with the single-scale problem. It can be observed that the total accumulated time for the Global-Local formulations took 849 s whereas the single-scale simulation took 19752 s. Hence, Global-Local formulations performs 23.3 times faster.

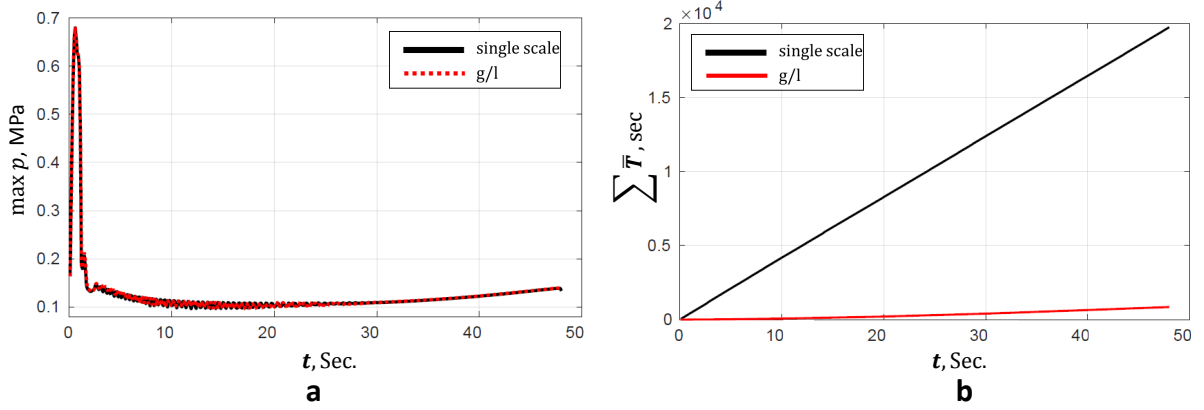


Figure 8: Example 1. Hydraulically induced crack driven by fluid volume injection. (a) Fluid pressure p within the crack region versus injection time; and (b) computational time-injection time curves in terms of the accumulated time.

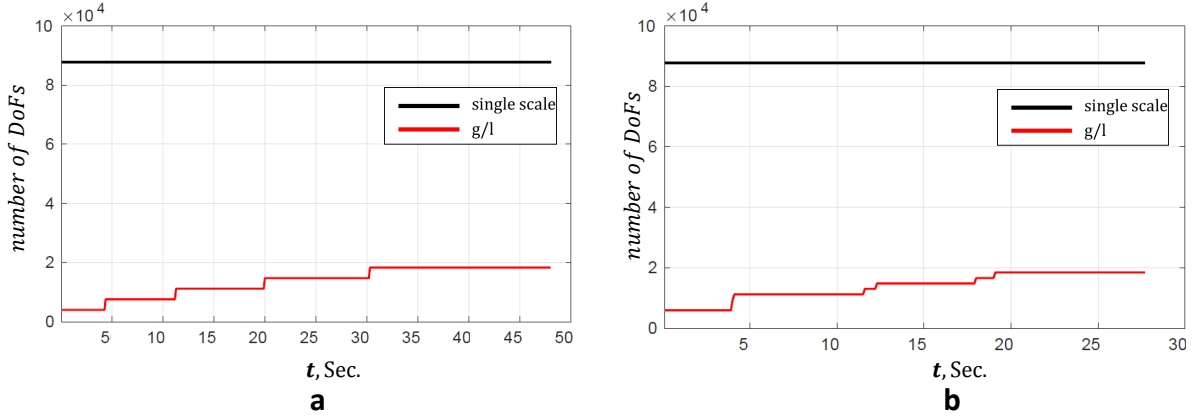


Figure 9: Number of degrees of freedom for the single scale problem and Global-Local formulation. (a) Example 1; and (b) Example 2.

Furthermore, for each jump in Fig. 9a, the predictor-corrector adaptive scheme is active and applied on the Global-Local scheme which increases the number of degrees of freedoms. At the complete failure state, i.e. $t = 48.5$ s, the total number of local nodes, elements and the degrees of freedoms are 5985, 5780 and 17955, respectively for the Global-local formulations. Whereas for the single-scale the number of nodes, elements and the degrees of freedoms are 29241, 28900 and 87723, respectively. Hence the Global-Local approach requires significantly less degrees of freedom, as shown in Fig. 9a.

4.2. Joining of two cracks driven by fluid volume injection

The second example is concerned with the capability of the proposed GL approach for handling *coalescence* and *merging* of *crack paths* in the local domains. Crack-initiation and curved-crack-propagation, representing a mixed-mode fracture, are predicted with a Global-Local formulation.

The geometrical setup and the loading conditions of the specimen is similar to the benchmark problem of [61] and depicted in Fig. 10. We keep all parameters and loading as in the previous example. The first crack \mathcal{C}_1 is located near the middle of the domain

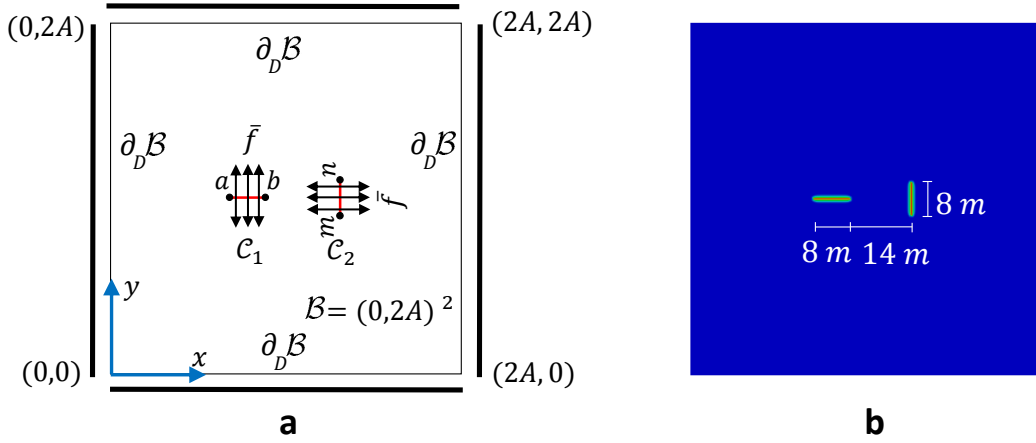


Figure 10: Joining of two cracks driven by fluid volume injection. (a) Geometry and boundary conditions; and (b) described crack phase-field d as a Dirichlet boundary conditions at $t = 0$ s.

with coordinates $a = (28, 40)$ and $b = (36, 40)$. The second crack \mathcal{C}_2 is vertically-oriented at $n = (50, 44)$ and $m = (50, 36)$ with a distance of 14 m from \mathcal{C}_1 . A constant fluid flow of $\bar{f} = 0.002$ m²/s is injected in \mathcal{C}_1 and \mathcal{C}_2 as sketched in Fig. 10. At the boundary $\partial_D \mathcal{B}$, all the displacements are fixed in both directions and the fluid pressure is set to zero. Fluid injection \bar{f} continues until failure for $T = 28$ s with time step $\Delta t = 0.1$ s during the simulation.

Figure 11 shows the evolutions of the fluid pressure p (first row) and the crack phase-field d (second row) for the single-scale problem at different times $[t = 1.8; 6.5; 13.5; 27.7$ s]. Here the crack propagates from the notches. We again observe nearly constant fluid pressure in the fractured area ($d = 1$), whereas outside the crack zone p is much lower, see 10 (first row).

The local-scale results with the corresponding mesh are depicted in Fig. 12 for different fluid injection stages. Hereby, the vertical displacement u_y (first row), fluid pressure p (second row), crack phase-field d (third row) and local domain (fourth row) evolutions of the Global-Local formulation are demonstrated in Fig. 6 for four time steps $[t = 1.8; 6.5; 13.5; 27.7$ s]. It is remarkably observed that the Global-Local approach augmented with predictor-corrector mesh adaptivity leads to the optimum number of elements to be used for the simulation, hence reducing additional cost. Additionally, note that extending the reservoir domain will significantly increase the computational cost for the single-scale problem (due to increase the number of elements) but this will not change the computational cost for Global-Local formulation, thus applicable for the real large structure. Therefore, localize effect (crack phase-field) which increase the computational cost is only considered within local domain and hence globally reduce the computational time. Another advantage of using the GL formulation is its capability of capturing the crack initiation and propagation at the homogenized global scale even with less number of elements as illustrated in Fig. 13.

Next, the maximum injected fluid pressure within the crack region is analyzed versus the fluid injection time in Figure 14a. The results obtained from Global-Local formulation are in a good agreement with the single scale solution. Figure 14b represents the

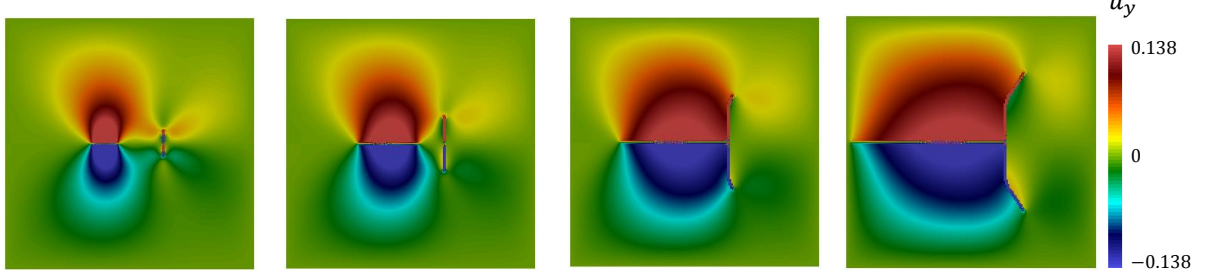
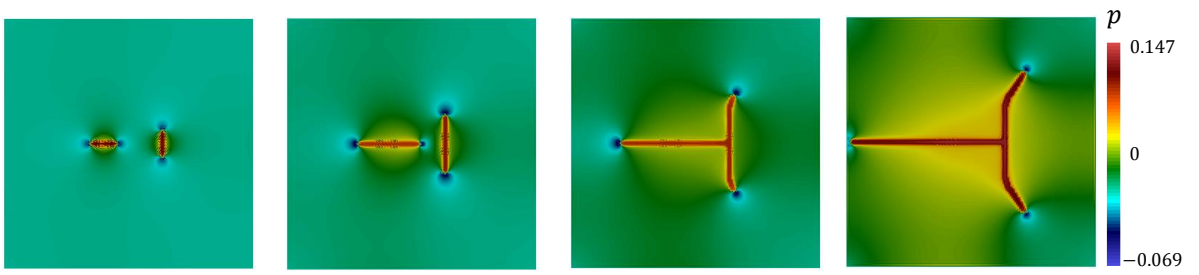
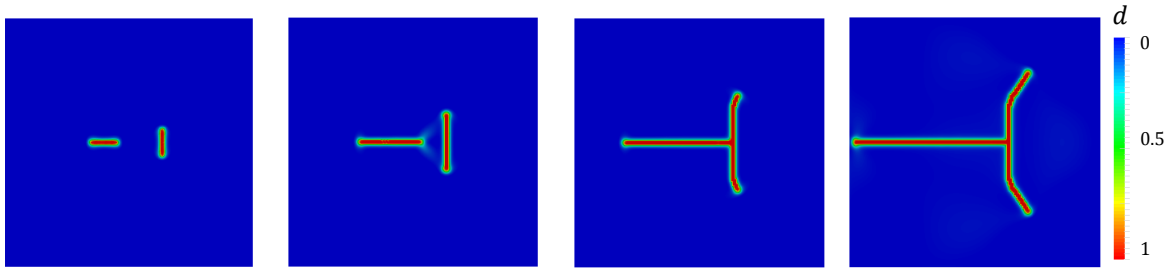
Single – scale vertical displacement**Single – scale pressure****Single – scale crack phase – field**

Figure 11: Example 2. Single-scale results of the joining cracks driven by fluid volume injection. Evolution of the vertical displacement u_y (first row), fluid pressure p (second row) and crack phase-field d (third row) for different deformation stages up to final failure at $[t = 1.8; 6.5; 13.5; 27.7 \text{ s}]$.

corresponding accumulative computational time (i.e. CPU simulation time), per injection fluid time. In this study, we observed that the total accumulated time for the GL approach took 529 s whereas the single-scale problem took 8784 s. Hence, Global-Local formulations performs 16.6 times faster.

Finally, Fig. 9b demonstrates the total number of degrees of freedoms versus the fluid injection time for GL scheme and the single-scale problem. At the complete failure state, i.e. $t = 27.7 \text{ sec}$, the total number of local nodes, elements and the degrees of freedoms for the GL method are 6036, 5780 and 18108, respectively. Whereas for the single-scale formulation the number of nodes, elements and the degrees of freedoms are 29241, 28900 and 87723, respectively. Thus the Global-Local approach requires significantly less degrees of freedom.

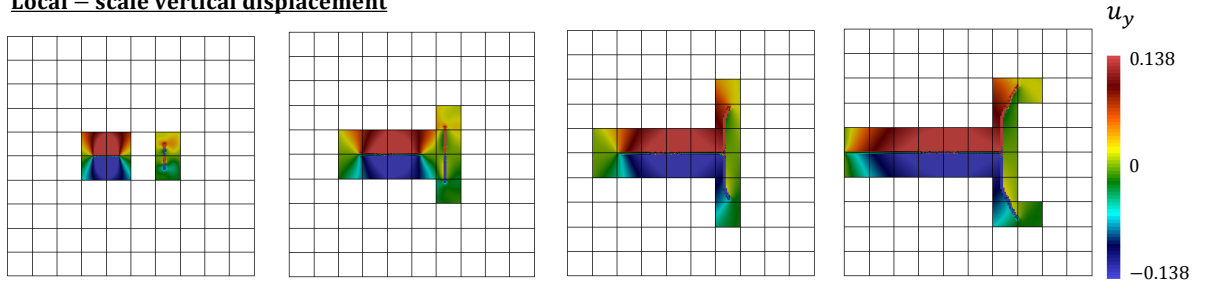
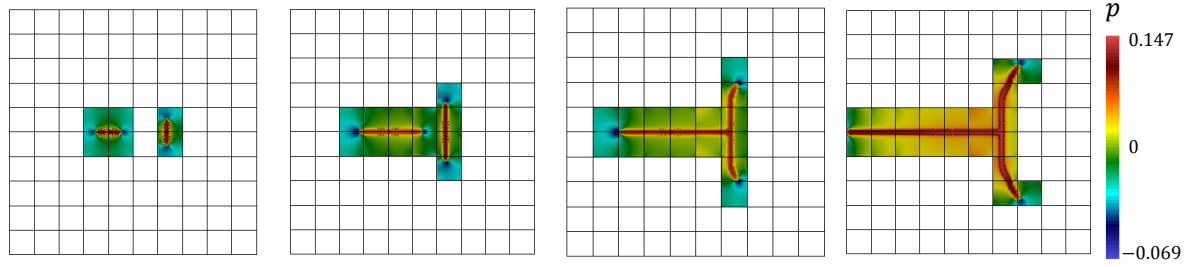
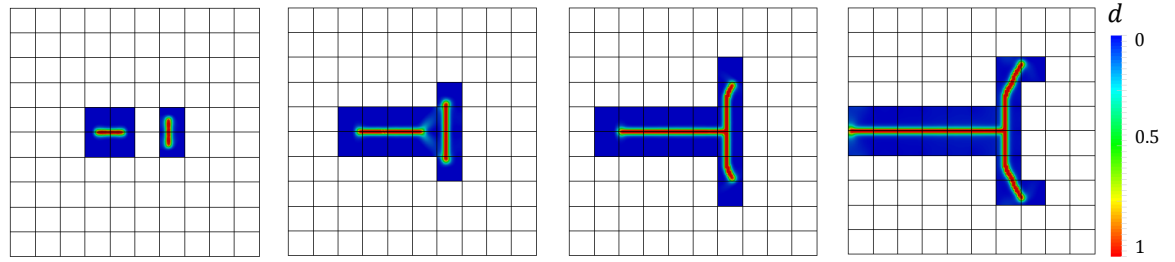
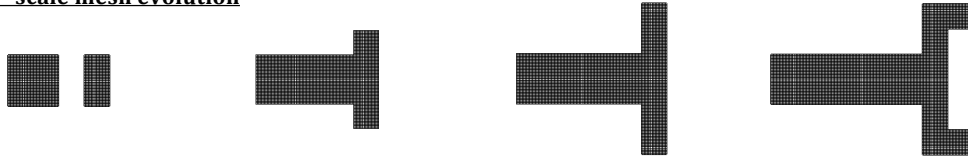
Local – scale vertical displacement**Local – scale pressure****Local – scale crack phase – field****Local – scale mesh evolution**

Figure 12: Example 2. Local-scale results of the joining cracks driven by fluid volume injection. Evolution of the vertical displacement u_y (first row), fluid pressure p (second row), crack phase-field d (third row) and local domain (fourth row) for different deformation stages up to final failure at $[t = 1.8; 6.5; 13.5; 27.7 \text{ s}]$.

5. Conclusion

In this work, we developed a global-local approach for pressurized fractures in porous media. This approach has the potential to tackle practical field problems in which a large reservoir might be considered and fracture propagation is a localized phenomenon.

First, we discussed the governing equations in Section 2. Then, we developed the main algorithm in Section 3. Therein, the coupling between the local and the global domain is formulated with Robin-type interface conditions. In our numerical tests, we have shown that the GL approach besides its feasibility for having two different finite element models for the global and local domain, enabled computations with legacy codes. Additionally, it required significantly less degrees of freedom than the single-scale formulation, leads to a remarkable reduction of the computational time. In this regard, the GL approach was 23

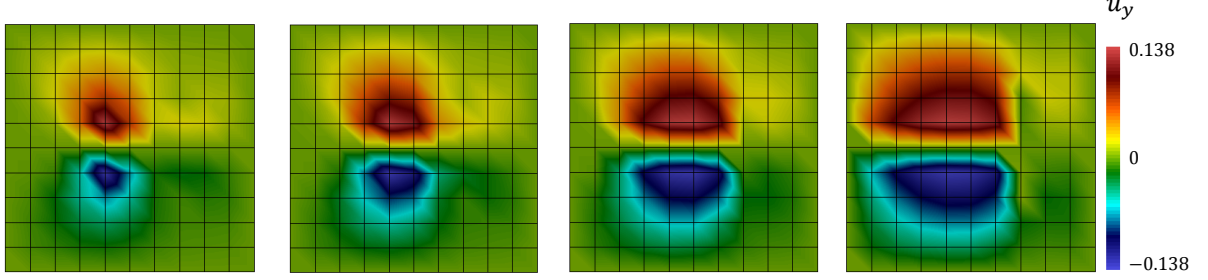
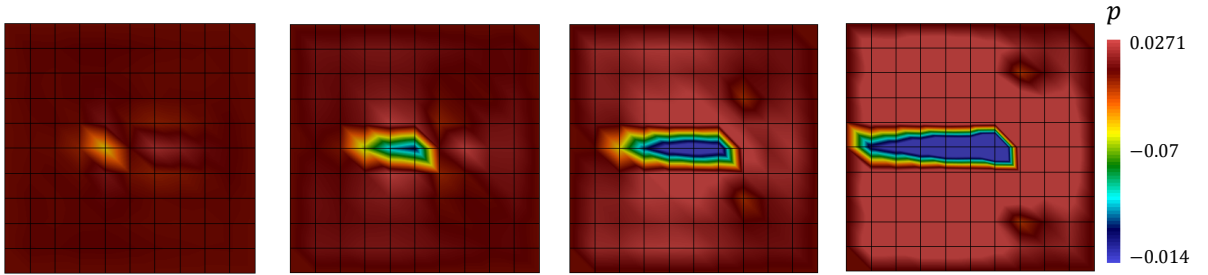
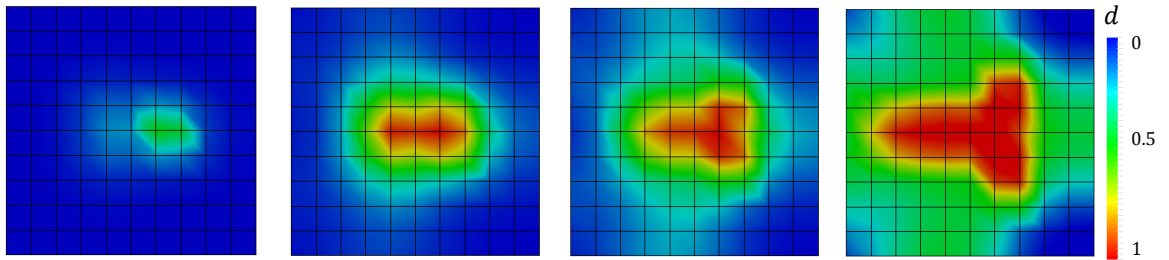
Global – scale vertical displacement**Global – scale pressure****Global – scale crack phase – field**

Figure 13: Example 2. Global-scale results of the joining cracks driven by fluid volume injection. Evolution of the vertical displacement u_y (first row), fluid pressure p (second row) and crack phase-field d (third row) for different fluid injection stages up to final failure at $[t = 1.8; 6.5; 13.5; 27.7 \text{ s}]$.

times faster than the standard phase-field formulation (single-scale solution) in the first example and 16 times faster in the second numerical test. Yet, an excellent performance of the proposed framework in all examples was observed.

Acknowledgment

F. Aldakheel was funded by the PRIORITY PROGRAM DFG - SPP 2020 within its second funding phase. N. Noii was partially supported by the PRIORITY PROGRAM DFG - SPP 1748. T. Wick and P. Wriggers were funded by the Deutsche Forschungsgemeinschaft (DFG, German Research Foundation) under Germany's Excellence Strategy within the CLUSTER OF EXCELLENCE PHOENIXD (EXC 2122).

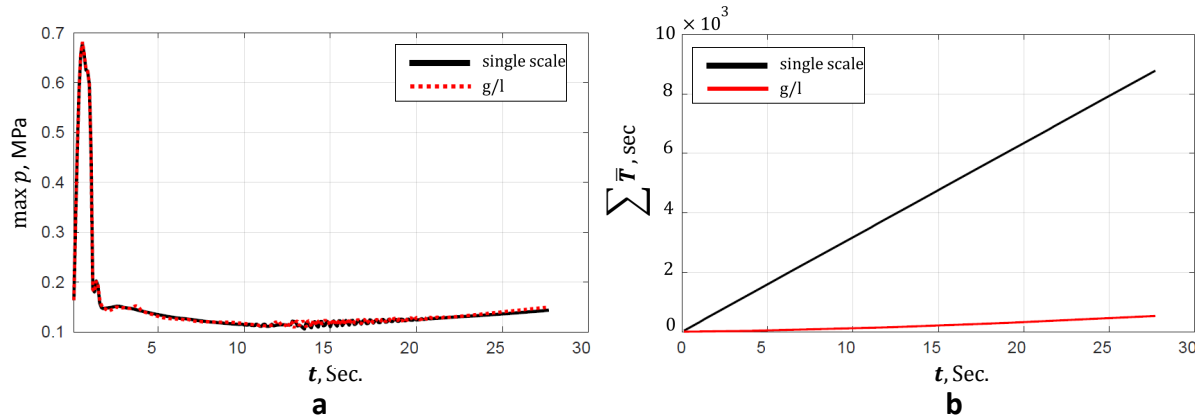


Figure 14: Example 2. Joining of two cracks driven by fluid volume injection. (a) Fluid pressure p within the crack region versus injection time; and (b) computational time-injection time curves in terms of the accumulated time.

References

- [1] ALDAKHEEL, F.; MAUTHE, S.; MIEHE, C. [2014]: *Towards phase field modeling of ductile fracture in gradient-extended elastic-plastic solids*. Proceedings in Applied Mathematics and Mechanics, 14: 411–412.
- [2] ALDAKHEEL, F.; HUDOBIVNIK, B.; HUSSEIN, A.; WRIGGERS, P. [2018]: *Phase-field modeling of brittle fracture using an efficient virtual element scheme*. Computer Methods in Applied Mechanics and Engineering, 341: 443–466.
- [3] ALDAKHEEL, F. [2016]: *Mechanics of Nonlocal Dissipative Solids: Gradient Plasticity and Phase Field Modeling of Ductile Fracture*. Ph.D. Thesis, Institute of Applied Mechanics (CE), Chair I, University of Stuttgart. <http://dx.doi.org/10.18419/opus-8803>.
- [4] ALDAKHEEL, F.; WRIGGERS, P.; MIEHE, C. [2018]: *A modified gurson-type plasticity model at finite strains: Formulation, numerical analysis and phase-field coupling*. Computational Mechanics, 62: 815–833.
- [5] ALDAKHEEL, F.; HUDOBIVNIK, B.; WRIGGERS, P. [2019]: *Virtual element formulation for phase-field modeling of ductile fracture*. International Journal for Multiscale Computational Engineering, 17(2): 181–200.
- [6] ALDAKHEEL, F.; TOMANN, C.; LOHAUS, L.; WRIGGERS, P. [2019]: *Water-induced failure mechanics for concrete*. Proceedings in Applied Mathematics and Mechanics, 19(1). <https://doi.org/10.1002/pamm.201900140>.
- [7] ARTINA, M.; FORNASIER, M.; MICHELETTI, S.; PEROTTO, S. [2015]: *Anisotropic mesh adaptation for crack detection in brittle materials*. SIAM J. Sci. Comput., 37(4): B633–B659.
- [8] BIOT, M. [1972]: *Theory of finite deformations of pourous solids*. Indiana University Mathematics Journal, 21: 597–620.
- [9] BOURDIN, B. [2007]: *Numerical implementation of the variational formulation for quasi-static brittle fracture*. Interfaces and free boundaries, 9: 411–430.
- [10] BOURDIN, B.; FRANCFORT, G.; MARIGO, J.-J. [2000]: *Numerical experiments in revisited brittle fracture*. Journal of the Mechanics and Physics of Solids, 48(4): 797–826.

-
- [11] BOURDIN, B.; CHUKWUDOZIE, C.; YOSHIOKA, K. [2012]: *A variational approach to the numerical simulation of hydraulic fracturing*. SPE Journal, Conference Paper 159154-MS.
 - [12] BRUN, M. K.; WICK, T.; BERRE, I.; NORDBOTTEN, J. M.; RADU, F. A. [2019]: *An iterative staggered scheme for phase field brittle fracture propagation with stabilizing parameters*. Accepted for publication in Comp. Meth. Appl. Mech. Engrg. (CMAME).
 - [13] BURKE, S.; ORTNER, C.; SÜLI, E. [2010]: *An adaptive finite element approximation of a variational model of brittle fracture*. SIAM J. Numer. Anal., 48(3): 980–1012.
 - [14] BURKE, S.; ORTNER, C.; SÜLI, E. [2013]: *An adaptive finite element approximation of a generalized Ambrosio-Tortorelli functional*. M3AS, 23(9): 1663–1697.
 - [15] CAJUHI, T.; SANAVIA, L.; DE LORENZIS, L. [2017]: *Phase-field modeling of fracture in variably saturated porous media*. Computational Mechanics.
 - [16] CHUKWUDOZIE, C.; BOURDIN, B.; YOSHIOKA, K. [2019]: *A variational phase-field model for hydraulic fracturing in porous media*. Computer Methods in Applied Mechanics and Engineering, 347: 957 – 982.
 - [17] COUSSY, O. [1995]: *Mechanics of porous continua*. Wiley.
 - [18] DANA, S.; WHEELER, M. F. [2018]: *Convergence analysis of two-grid fixed stress split iterative scheme for coupled flow and deformation in heterogeneous poroelastic media*. Computer Methods in Applied Mechanics and Engineering, 341: 788 – 806.
 - [19] DANA, S.; GANIS, B.; WHEELER, M. F. [2018]: *A multiscale fixed stress split iterative scheme for coupled flow and poromechanics in deep subsurface reservoirs*. Journal of Computational Physics, 352: 1 – 22.
 - [20] DE BOER, R.; EHLERS, W. [1990]: *The development of the concept of effective stresses*. Acta Mechanica, 83(1-2): 77–92.
 - [21] DE BOER, R. [2000]: *Theory of porous media: highlights in historical development and current state*. Springer Science & Business Media.
 - [22] DITTMANN, M.; ALDAKHEEL, F.; SCHULTE, J.; WRIGGERS, P.; HESCH, C. [2018]: *Variational phase-field formulation of non-linear ductile fracture*. Computer Methods in Applied Mechanics and Engineering, 342: 71–94.
 - [23] EHLERS, W. [2002]: *Foundations of multiphase and porous materials*, pp. 3–86. Springer Berlin Heidelberg, Berlin, Heidelberg.
 - [24] EHLERS, W.; LUO, C. [2017]: *A phase-field approach embedded in the theory of porous media for the description of dynamic hydraulic fracturing*. Computer Methods in Applied Mechanics and Engineering, 315: 348–368.
 - [25] FARHAT, C.; ROUX, F. [1991]: *A method of finite element tearing and interconnecting and its parallel solution algorithm*. International Journal for Numerical Methods in Engineering, 32: 1205–1227.
 - [26] FISH, J. [2014]: *Practical Multiscale*. John Wiley and Sons, Ltd., United Kingdom.
 - [27] FRANCFORT, G.; MARIGO, J.-J. [1998]: *Revisiting brittle fracture as an energy minimization problem*. Journal of the Mechanics and Physics of Solids, 46(8): 1319–1342.
 - [28] GENDRE, L.; ALLIX, O.; GOSSELET, P.; COMTE, F. [2009]: *Non-intrusive and exact global/local techniques for structural problems with local plasticity*. Computational Mechanics, 44: 233–245.
 - [29] GERASIMOV, T.; LORENZIS, L. D. [2016]: *A line search assisted monolithic approach for phase-field computing of brittle fracture*. Computer Methods in Applied

- Mechanics and Engineering, 312: 276–303.
- [30] GERASIMOV, T.; NOH, N.; ALLIX, O.; DE LORENZIS, L. [2018]: *A non-intrusive global/local approach applied to phase-field modeling of brittle fracture*. Advanced Modeling and Simulation in Engineering Sciences. <https://doi.org/10.1186/s40323-018-0105-8>.
 - [31] GIRAULT, V.; PENCHEVA, G.; WHEELER, M. F.; WILDEY, T. [2011]: *Domain decomposition for poroelasticity and elasticity with dg jumps and mortars*. Mathematical Models and Methods in Applied Sciences, 21(1): 169–213.
 - [32] GIRAULT, V.; WHEELER, M. F.; ALMANI, T.; DANA, S. [2019]: *A priori error estimates for a discretized poro-elastic-elastic system solved by a fixed-stress algorithm*. Oil Gas Sci. Technol. Rev IFP Energies nouvelles, 24.
 - [33] GIRAULT, V.; PENCHEVA, G. V.; WHEELER, M. F.; WILDEY, T. M. [2009]: *Domain decomposition for linear elasticity with dg jumps and mortars*. Computer Methods in Applied Mechanics and Engineering, 198(21): 1751 – 1765. Advances in Simulation-Based Engineering Sciences - Honoring J. Tinsley Oden.
 - [34] GOSSELET, P.; REY, C. [2006]: *Non-overlapping domain decomposition methods in structural mechanics*. Archives of Computational Methods in Engineering, 13: 515–572.
 - [35] HEIDER, Y.; SUN, W. [2019]: *A phase field framework for capillary-induced fracture in unsaturated porous media: Drying-induced vs. hydraulic cracking*. Computer Methods in Applied Mechanics and Engineering. <https://doi.org/10.1016/j.cma.2019.112647>.
 - [36] HEIDER, Y.; REICHE, S.; SIEBERT, P.; MARKERT, B. [2018]: *Modeling of hydraulic fracturing using a porous-media phase-field approach with reference to experimental data*. Engineering Fracture Mechanics, 202: 116 – 134.
 - [37] HEISTER, T.; WHEELER, M. F.; WICK, T. [2015]: *A primal-dual active set method and predictor-corrector mesh adaptivity for computing fracture propagation using a phase-field approach*. Computer Methods in Applied Mechanics and Engineering, 290: 466 – 495.
 - [38] HEISTER, T.; WICK, T. [2018]: *Parallel solution, adaptivity, computational convergence, and open-source code of 2d and 3d pressurized phase-field fracture problems*. PAMM, 18(1): e201800353.
 - [39] LEE, S.; WHEELER, M. F.; WICK, T. [2016]: *Pressure and fluid-driven fracture propagation in porous media using an adaptive finite element phase field model*. Computer Methods in Applied Mechanics and Engineering, 305: 111 – 132.
 - [40] LEE, S.; MIKELIC, A.; WHEELER, M.; WICK, T. [2018]: *Phase-field modeling of two phase fluid filled fractures in a poroelastic medium*. Multiscale Modeling & Simulation, 16(4): 1542–1580.
 - [41] LEE, S.; MIKELIĆ, A.; WHEELER, M. F.; WICK, T. [2016]: *Phase-field modeling of proppant-filled fractures in a poroelastic medium*. Computer Methods in Applied Mechanics and Engineering, 312: 509 – 541.
 - [42] LEE, S.; WHEELER, M. F.; WICK, T.; SRINIVASAN, S. [2017]: *Initialization of phase-field fracture propagation in porous media using probability maps of fracture networks*. Mechanics Research Communications, 80: 16 – 23. Multi-Physics of Solids at Fracture.
 - [43] LEE, S.; MIN, B.; WHEELER, M. F. [2018]: *Optimal design of hydraulic fracturing in porous media using the phase field fracture model coupled with genetic algorithm*.

- Computational Geosciences, 22(3): 833–849.
- [44] MANG, K.; WICK, T. [2019]: *Numerical methods for variational phase-field fracture problems*. Lecture notes at Leibniz University Hannover, doi: <https://doi.org/10.15488/5129>.
 - [45] MARKERT, B. [2007]: *A constitutive approach to 3-d nonlinear fluid flow through finite deformable porous continua*. Transport in Porous Media, 70(3): 427.
 - [46] MIEHE, C.; HOFACKER, M.; SCHÄNZEL, L.-M.; ALDAKHEEL, F. [2015]: *Phase field modeling of fracture in multi-physics problems. Part II. brittle-to-ductile failure mode transition and crack propagation in thermo-elastic-plastic solids*. Computer Methods in Applied Mechanics and Engineering, 294: 486–522.
 - [47] MIEHE, C.; MAUTHE, S. [2016]: *Phase field modeling of fracture in multi-physics problems. part iii. crack driving forces in hydro-poro-elasticity and hydraulic fracturing of fluid-saturated porous media*. Computer Methods in Applied Mechanics and Engineering, 304: 619–655.
 - [48] MIEHE, C.; MAUTHE, S.; TEICHTMEISTER, S. [2015]: *Minimization principles for the coupled problem of darcy-biot-type fluid transport in porous media linked to phase field modeling of fracture*. Journal of the Mechanics and Physics of Solids, 82: 186 – 217.
 - [49] MIEHE, C.; ALDAKHEEL, F.; TEICHTMEISTER, S. [2017]: *Phase-field modeling of ductile fracture at finite strains: A robust variational-based numerical implementation of a gradient-extended theory by micromorphic regularization*. International Journal for Numerical Methods in Engineering, 111(9): 816–863.
 - [50] MIKELIĆ, A.; WHEELER, M. F.; WICK, T. [2015]: *A phase-field method for propagating fluid-filled fractures coupled to a surrounding porous medium*. SIAM Multiscale Model. Simul., 13(1): 367–398.
 - [51] MIKELIĆ, A.; WHEELER, M. F.; WICK, T. [2015]: *A quasi-static phase-field approach to pressurized fractures*. Nonlinearity, 28(5): 1371–1399.
 - [52] MIKELIĆ, A.; WHEELER, M. F.; WICK, T. [2019]: *Phase-field modeling through iterative splitting of hydraulic fractures in a poroelastic medium*. GEM - International Journal on Geomathematics, 10(1). <https://doi.org/10.1007/s13137-019-0113-y>.
 - [53] MOTA, A.; TEZAUR, I.; ALLEMAN, C. [2017]: *The schwarz alternating method in solid mechanics*. Computer Methods in Applied Mechanics and Engineering, 319: 19–51.
 - [54] NOII, N.; ALDAKHEEL, F.; WICK, T.; WRIGGERS, P. [2019]: *An adaptive global-local approach for phase-field modeling of anisotropic brittle fracture*. Computer Methods in Applied Mechanics and Engineering. <https://doi.org/10.1016/j.cma.2019.112744>.
 - [55] NOII, N.; WICK, T. [2019]: *A phase-field description for pressurized and non-isothermal propagating fractures*. Computer Methods in Applied Mechanics and Engineering, 351: 860 – 890.
 - [56] SCHREFLER, B. A.; SECCHI, S.; SIMONI, L. [2006]: *On adaptive refinement techniques in multi-field problems including cohesive fracture*. Computer Methods in Applied Mechanics and Engineering, 195(4): 444 – 461. Adaptive Modeling and Simulation.
 - [57] SEITZ, A.; FARAH, P.; KREMHELLER, J.; WOHLMUTH, B. I.; WALL, W. A.; POPP, A. [2016]: *Isogeometric dual mortar methods for computational contact mechanics*. Computer Methods in Applied Mechanics and Engineering, 301: 259–280.

-
- [58] SINGH, N.; VERHOOSSEL, C.; BRUMMELEN, E. VAN [2018]: *Finite element simulation of pressure-loaded phase-field fractures*. *Meccanica*, 53(6): 1513–1545.
 - [59] TERZAGHI, K. [1943]: *Theoretical soil mechanics*. *johnwiley & sons*. New York, pp. 11–15.
 - [60] WANG, K.; SUN, W. [2017]: *A unified variational eigen-erosion framework for interacting brittle fractures and compaction bands in fluid-infiltrating porous media*. *Computer Methods in Applied Mechanics and Engineering*, 318: 1–32.
 - [61] WHEELER, M.; WICK, T.; WOLLNER, W. [2014]: *An augmented-lagrangian method for the phase-field approach for pressurized fractures*. *Computer Methods in Applied Mechanics and Engineering*, 271: 69–85.
 - [62] WICK, T. [2016]: *Goal functional evaluations for phase-field fracture using PU-based DWR mesh adaptivity*. *Computational Mechanics*, 57(6): 1017–1035.
 - [63] WICK, T. [2017]: *Modified Newton methods for solving fully monolithic phase-field quasi-static brittle fracture propagation*. *Computer Methods in Applied Mechanics and Engineering*, 325: 577 – 611.
 - [64] WICK, T. [2017]: *An error-oriented Newton/inexact augmented Lagrangian approach for fully monolithic phase-field fracture propagation*. *SIAM Journal on Scientific Computing*, 39(4): B589–B617.
 - [65] WICK, T.; SINGH, G.; WHEELER, M. [2016]: *Fluid-filled fracture propagation using a phase-field approach and coupling to a reservoir simulator*. *SPE Journal*, 21(03): 981–999.
 - [66] WILSON, Z. A.; LANDIS, C. M. [2016]: *Phase-field modeling of hydraulic fracture*. *Journal of the Mechanics and Physics of Solids*, 96: 264 – 290.
 - [67] WOHLMUTH, B. [2011]: *Variationally consistent discretization schemes and numerical algorithms for contact problems*. *Acta Numerica*, 20: 569–734.
 - [68] WOHLMUTH, B. [2000]: *A mortar finite element method using dual spaces for the lagrange multiplier*. *SIAM Journal on Numerical Analysis*, 38.
 - [69] WOHLMUTH, B. [2002]: *A comparison of dual lagrange multiplier spaces for mortar finite element discretizations*. *ESAIM: Mathematical Modelling and Numerical Analysis - Modélisation Mathématique et Analyse Numérique*, 36(6): 995–1012.
 - [70] XIA, L.; YVONNET, J.; GHABEZLOO, S. [2017]: *Phase field modeling of hydraulic fracturing with interfacial damage in highly heterogeneous fluid-saturated porous media*. *Engineering Fracture Mechanics*, 186: 158–180.